

Intergranular Pressure Solution in NaCl: Grain-to-Grain Contact Experiments under the Optical Microscope

P.M.T.M. Schutjens¹ and C.J. Spiers²

¹ Shell International Exploration and Production BV, Volmerlaan 8, PO Box 60, 2280 AB Rijswijk - The Netherlands

² HPT Laboratory, Faculty of Earth Sciences, Utrecht University, PO Box 80 021, 3508 TA Utrecht - The Netherlands

e-mail: p.m.t.schutjens@siep.shell.com - cspiers@geo.uu.nl

Résumé — Dissolution sous contrainte dans NaCl : expériences de contact grain à grain sous microscope optique — La dissolution sous contrainte (*IPS - Intergranular Pressure Solution*) représente un mécanisme de lithification, de compaction et de déformation à l'échelle géologique pour une large gamme de roches. Les études expérimentales d'IPS réalisées sur des agrégats de quartz n'ont pas été couronnées de succès en raison d'un taux faible d'IPS, et les expériences IPS réalisées en utilisant une halite saturée comme analogue de roche (Spiers et Schutjens, 1990 ; Hickman et Evans, 1991) ont laissé des incertitudes quant au détail des mécanismes IPS et à la structure/saturation au contact du grain dans ce matériau. La présente étude fait état de quatre expériences de dissolution de contact réalisées sous microscope optique afin d'étudier le mécanisme et la cinétique de l'IPS pour des contacts simples halite/halite et halite/verre, chargés en eau salée (température ambiante). Des forces normales de contact dans la gamme de 1,0 à 2,6 N ont été appliquées en présence d'eau salée saturée en NaCl, induisant des pressions de 0,8 à 7,4 MPa. Des pertes de masse et des convergences — fonction du temps — ont été observées pour tous les contacts. Dans tous les cas, le fait de charger le contact (ou d'augmenter la charge sur le contact) a conduit à la formation immédiate d'une morphologie de contact rugueuse, composée d'un motif d'îles et de canaux, contrôlé par des caractéristiques cristallographiques, à l'échelle de quelques microns. Cette microstructure non équilibrée a évolué dans le temps vers une face de contact optiquement plate. Le processus de convergence/lissage doit donc avoir compris une diffusion de masse en dehors du contact et une expulsion de la saumure par l'intermédiaire d'une phase d'eau salée connectée, à l'intérieur du contact. Le fait qu'une structure rugueuse à petite échelle ait persisté dans des contacts ayant évolué vers un aspect optiquement plat n'est pas établi, bien que les observations au microscope à balayage électronique faites après l'essai le suggèrent. Si ce phénomène était confirmé, son amplitude serait inférieure à 500 nm. Les mesures des taux de dissolution ont permis une comparaison avec un modèle pour l'IPS. Les analyses suggèrent que la diffusion en solution, à travers le contact, contrôlait certainement le taux. La structure du contact et la diffusivité varient alors avec la force de contact et la convergence. Les résultats sont largement en adéquation avec ceux des expériences précédentes sur la compaction, réalisées en utilisant de la poudre d'halite saturée. Les divergences avec les résultats d'autres chercheurs, issus d'expériences de dissolution sur des contacts simples, peuvent être expliquées en termes de différence de configuration d'expérience et de concurrence entre les forces motrices.

Mots-clés : dissolution sous pression, contact de grain, diffusion, dissolution de l'halite.

Abstract—Intergranular Pressure Solution in NaCl: Grain-to-Grain Contact Experiments under the Optical Microscope—Intergranular Pressure Solution (IPS) is an important geologic lithification, compaction and deformation mechanism in a wide variety of crustal rocks. Experimental studies of IPS in quartz aggregates have not been very successful due to the low rate of IPS, and IPS experiments performed using wet halite as a rock analogue (Spiers and Schutjens, 1990; Hickman and Evans, 1991) have left uncertainty about the detailed IPS mechanism and grain contact structure/wetting in this material. The present study reports four contact dissolution experiments performed under the optical microscope to study the mechanism and kinetics of IPS at single halite/halite and halite/glass contacts loaded under brine (room temperature). Normal constant contact forces in the range 1.0 to 2.6 N were applied in the presence of NaCl-saturated brine, exerting stresses of 0.8 to 7.4 MPa. Time-dependent mass removal and convergence were observed at all contacts. In all cases, loading of the contact (or increasing the load on the contact) led to instantaneous formation of a rough contact morphology, composed of a crystallographically-controlled pattern of islands and channels with a length scale of several micrometers. This nonequilibrium microstructure evolved with time to an optically flat contact face while contact broadening and convergence continued. The smoothing/convergence process must therefore have involved diffusion of mass out of the contact, and expulsion of brine, through a connected brine phase within the contact. Whether a fine-scale rough structure persisted in contacts which evolved to optical flatness is not known, though post-test SEM (Scanning Electron Microscopy) observations suggest that it may have. If so, its amplitude was less than 500 nm. Measurements of dissolution rates enabled comparison with a model for IPS. The analysis suggests that solute diffusion through the contact boundary was probably rate-controlling, with the contact structure and effective diffusivity varying with contact force and on-going convergence. The results agree broadly with those of previous compaction creep experiments performed using wet halite powder. Discrepancies with other workers results for single-contact dissolution experiments can be explained in terms of differences in experimental configuration and competition between driving forces.

Keywords: pressure solution, grain contact, diffusion, halite dissolution.

ABBREVIATIONS

C	concentration of solute in grain boundary fluid (kg/m^3)
D	intrinsic diffusivity of solute in grain boundary fluid (m^2/s)
F	contact force applied by dead weight (N)
h	average grain boundary width (m)
J	volumetric flux vector (general) ($\text{kg}/\text{m}^2\cdot\text{s}$)
L	length of rectangular contact surface area (m)
P_e	effective confining pressure (MPa)
r	negative radius of curvature at grain contact margins (m)
R	universal gas constant (8.314) ($\text{J}/\text{mol}\cdot\text{K}$)
S	effective grain boundary width, with $S = h(1 - \alpha)$ (m)
T	absolute temperature ($^\circ\text{K}$)
V	molar volume of the solid phase (m^3/mol)
W	width of rectangular contact surface area (m)
\dot{W}	widening rate of short edge W of surface area (“contact spreading rate”) (m/s)
x	distance along the short edge of the contact surface area (m)
\dot{X}	convergence rate (m/s)
Z	kinetic coefficient = $D\cdot C_0\cdot S$ (kg/s)

Greek Symbols

α	area fraction of grain boundary occupied by solid (“islands”)
----------	---------------------------------------------------------------

Δ_c	rate of energy input to the grain contact (force times convergence rate) (J/s)
Δ_{gb}	rate of energy dissipation by solute diffusion in dilute grain boundary fluid (J/s)
γ	interfacial energy halite crystal and NaCl-saturated brine (J/m^2)
μ	chemical potential of solute in solution (J/kg)
$\Delta\mu_{ng}$	driving force (potential drop) for neck growth (J/kg)
$\Delta\mu_{ps}$	driving force (potential drop) for pressure solution (J/kg)
ρ	solid density (kg/m^3)
σ_n	effective normal stress at contact (Pa)
Λ	energy dissipation rate per unit volume ($\text{J}/\text{m}^3\cdot\text{s}$)
Ω	molar volume (m^3/mol).

INTRODUCTION

On the basis of petrographic and microstructural observations, stress-related dissolution of material within grain contacts, or Intergranular Pressure Solution (IPS), is considered an important lithification, compaction and deformation mechanism in low-grade metamorphic rocks (Rutter, 1983; Houseknecht, 1984, 1987, 1988; Bell and Cuff, 1989; Tada and Siever, 1989). IPS is also recognized as one of the main factors controlling the geological evolution of porosity and permeability, and hence capacity and productivity, of (potential) hydrocarbon

reservoirs (Pittman, 1979; Hutcheon, 1983; Carozzi and Von Bergen, 1987), as well as a possible mechanism controlling fault creep, fault gouge compaction and fault strength recovery (Rutter and Mainprice, 1978; Angevine *et al.*, 1982; Lehner and Bataille, 1984; Sleep and Blanpied, 1992; Sleep, 1995). In addition, Urai *et al.* (1986) and Spiers *et al.* (1989, 1990) have shown that IPS can be an important deformation mechanism in halite rock at low strain rates, which has important implications for the design of waste repositories in rock salt formations, and for understanding salt tectonics. Clearly, then, a fundamental understanding of compaction and deformation by IPS is of substantial interest in petroleum geology, structural/metamorphic geology and tectonophysics.

This interest in IPS processes has provided an incentive for the development of numerous microphysical models for IPS and flow laws for compaction and deformation by IPS creep (Rutter, 1976, 1983; Raj, 1982; Lehner and Bataille, 1984; Lehner, 1990, 1995; Spiers and Schutjens, 1990; Gratz, 1991; Mullis, 1991; Paterson, 1995; Shimizu, 1995). By comparison with petrographic information on IPS, two broad classes of grain scale IPS mechanism have been proposed. The first is the so-called marginal dissolution process envisaged to involve progressive undercutting of grain contacts, coupled with plastic deformation and/or crushing of the contacts (Bathurst, 1958; Pharr and Ashby, 1983; Tada *et al.*, 1987). The second is the grain boundary diffusion mechanism, involving dissolution and diffusion of material through a dynamically stable, intergranular, fluid-filled island-channel network (Lehner, 1990, 1995; Spiers and Schutjens, 1990) or through a very thin adsorbed-fluid film (Weyl, 1959; Rutter, 1976, 1983; Hickman and Evans, 1995).

Many experimental investigations have been conducted to demonstrate the operation of IPS in the laboratory, to identify the mechanism and to quantify the rate of the process. Compaction creep experiments performed on wet quartz sand at effective stresses up to several tens of MPa and temperatures up to 400°C have met with only limited success in this respect: limited or ambiguous microstructural evidence for IPS has generally been found, and the mechanical data are inconsistent with models for IPS as rate-controlling mechanism (Renton *et al.*, 1969; De Boer *et al.*, 1977; Schutjens, 1991a; Dewers and Hajash, 1995). However, compaction experiments performed on fine grained quartz powder at 1200°K by Cox and Paterson (1991) have produced convincing microstructural evidence for IPS and for the existence of an island-channel structure within dissolving quartz grain contacts.

Compaction tests on brine-saturated halite aggregates, performed at relatively low stresses (≤ 5 MPa) and room temperature, have generally been more successful than experimental work on quartz, and have provided clear microstructural evidence for pervasive IPS manifested by grain indentations, grain contact truncations and euhedral overgrowths, and a “rough” fluid-invaded, island-channel

type grain boundary structure with an estimated thickness of several hundred nanometers (Spiers and Schutjens, 1990; Spiers *et al.*, 1990). Also good agreement was obtained with models for grain boundary diffusion controlled IPS (Spiers and Schutjens, 1990; Spiers *et al.*, 1990, Spiers and Brzesowsky, 1993). However, the observed microstructures in wet-compacted halite are “end product” microstructures. Accordingly, the possibility that much of the early strain was achieved by subsequently obscured marginal dissolution processes cannot be ruled out. Also, the structure and thickness of the grain boundary *during* IPS is not known, and may have been modified during unloading and extraction of the samples from the compaction vessel, for example due to grain boundary fracturing, precipitation of NaCl from the brine due to evaporation, or surface-energy driven solution/precipitation reactions in residual grain boundary fluid (Hickman and Evans, 1991). Knowledge of the grain boundary structure and thickness *during deformation* is essential for an understanding of grain boundary diffusion controlled IPS.

In addition to these uncertainties, Hickman and Evans (1991, 1992, 1995) obtained very different experimental results for IPS in halite, and drew the interpretations of Spiers, Schutjens and coworkers into question. Hickman and Evans (1991, 1992, 1995) measured deformation at the contacts between polished lenses of halite and polished plates of either halite or fused silica in the presence of saturated NaCl brine. When two halite lenses were pressed together, no IPS occurred but the halite-halite contacts gradually widened by neck growth. In contrast, when halite and silica were pressed together, IPS did occur. The neck growth at halite-halite contacts was interpreted by Hickman and Evans as evidence that the wetting angles were not zero, from which they deduced that there can be no continuous fluid film in the boundary between two halite crystals loaded under brine, and hence no steady-state IPS. Thus the results and interpretation of Hickman and Evans contrast sharply with the observations of Spiers and Schutjens (1990) and Spiers *et al.* (1990)—and call for more experiments in which the grain contact processes can be observed *during* deformation.

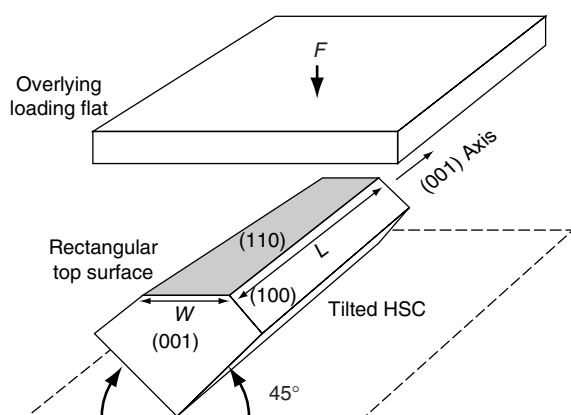
The present study reports four contact dissolution experiments performed under the optical microscope and designed to study the mechanism of dissolution at single halite/halite and halite/glass contacts loaded under brine. Measurements of dissolution rates enabled direct comparison with a model for diffusion-controlled IPS.

1 THEORETICAL CONSIDERATIONS

1.1 Principle of the Present Experiments

The experiments reported here attempt to dissolve away the edge of cleaved prismatic halite single crystals by loading them under brine against the (100) face of “partner” halite

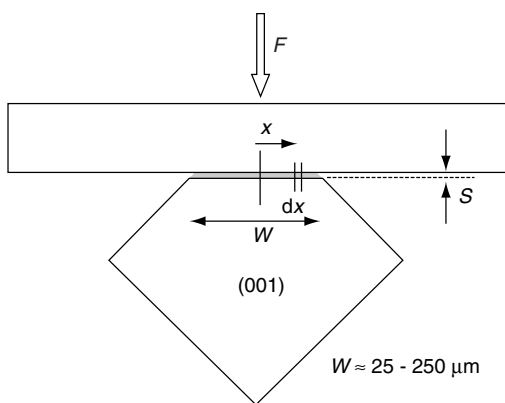
crystals (three experiments) or against a glass slide (one experiment). The experiments were conducted under the optical microscope. A schematic diagram of the sample configuration and geometry expected to result from IPS is shown in Figure 1. The wafer-shaped upper halite crystal or glass plate is brought into contact with the top edge of the lower crystal, and transmits a normal force F to the contact.



a

Figure 1a

Schematic diagram showing geometry and orientation of the cleaved halite single crystals (HSC) used in the present contact dissolution experiments. The rectangular (110) top face of the prismatic halite crystal is loaded against the (100) face of a wafer-shaped halite crystal (experiments T1-T3) or glass plate (T4) (see text). Note that in the case of convergence by dissolution of the prismatic crystal against the overlying flat plate, the convergence rate \dot{X} is proportional to the contact spreading rate \dot{W} , i.e. $\dot{X} = \dot{W}/2$.



b

Figure 1b

Cross-section normal to the crystal length L , illustrating the notation used in model derivation. No stress concentration occurs along the sharp lower edge of the prismatic crystal: it was pressed in a layer of epoxy, and is supported to its side by small halite cubes (Fig. 2).

Assuming that IPS occurs by diffusive mass transfer from the top edge of the lower crystal to the available free surface, and assuming no mass removal from the overlying plate, the vertical convergence rate \dot{X} is proportional to the rate \dot{W} at which the contact width W increases with time, i.e. $\dot{X} = \dot{W}/2$. For small displacements there is negligible overgrowth on the free surfaces, and so \dot{X} due to IPS can be calculated from optical measurements of W as a function of time. In addition, since the transmitted light beam is orthogonal to the crystal contact plane, the *internal* contact boundary microstructure can be observed during dissolution, as far as optical techniques allow. Note that in each experiment two prism/plate contact assemblies (Fig. 1) were loaded simultaneously by the same dead weight.

1.2 Microphysical Models: Assumptions and Starting Point

Before proceeding to describe our experiments, we present a model for crystal convergence by the anticipated mechanism of grain boundary diffusional IPS, previously identified as the rate-controlling mechanism during compaction creep of wet polycrystalline halite (Spiers *et al.*, 1990; Spiers and Schutjens, 1990). The model is developed for the geometry shown in Figure 1, and is based on the following assumptions:

- Removal of material from the loaded contact occurs purely by diffusion-controlled grain boundary diffusional IPS, i.e. all work done by the contact force F is dissipated in driving steady-state diffusion of dissolved material through the contact zone to the fluid surrounding the crystals. In accordance with previous work (see Rutter, 1976; Lehner, 1990, 1995; Spiers and Schutjens, 1990) this is equivalent to assuming that the “grain scale” driving force for transport by IPS is given by: $\Delta\mu_{ps} \approx \Delta\sigma_n/\rho$, where $\Delta\mu_{ps}$ (J/kg) is the chemical potential drop between source and sink sites, $\Delta\sigma_n$ (Pa) is the corresponding difference in effective normal stress, and ρ (kg/m³) is the density of the solid. Increases in free energy and hence chemical potential related to elastic or dislocation-stored energy are negligible in comparison to this driving force. This assumption of $\Delta\mu_{ps} \approx \Delta\sigma_n/\rho$ is the core of our model, as will be shown below.
- Precipitation occurs uniformly on the free surfaces, i.e. not inside the crystal contact zone or at the contact margin, so that the approximation $\dot{X} = \dot{W}/2$ is valid and the length of the contact (L) remains approximately constant.
- Only the edge of the lower halite crystal dissolves, and is thus truncated against the upper halite crystal or glass slide, in accordance with many of the IPS microstructures observed in wet-compacted halite aggregates (Spiers and Schutjens, 1990; Spiers *et al.*, 1990).
- The contact zone possesses a stable thin film or dynamically-stable island-channel structure, allowing access for the solution phase while simultaneously transmitting the applied load across the contact.

– Any shear stresses developed along the contact are neglected.

Two possible diffusion pathways will be considered. In Model A (Fig. 1a), the rate-controlling diffusion of material is assumed to occur parallel to the short edge W of the contact interface (i.e., along the (110) direction, cf. an infinite bar). In Model B (Fig. 1b), diffusion is assumed to occur parallel to the long edge L of the contact interface (i.e., along the (001) direction) to allow for the possibility of crystallographically controlled anisotropic diffusion.

1.3 Model A (Diffusion Parallel to the Short Edge of the Contact Interface)

The present analysis is based on consideration of mass balance and dissipation balance in the grain contact where IPS is assumed to occur, and is equivalent to the analysis employed by previous authors for circular contacts (Rutter, 1976; Lehner 1990, 1995; Spiers and Schutjens, 1990). With reference to Figure 1b, the mass input into a central strip of the contact zone of width $2x$ (region $\pm x$), via dissolution of the bottom crystal, must balance the diffusive flux out of the strip under steady-state conditions (i.e. solute concentration is fixed in time), so that:

$$2xL\dot{X}\rho = 2JLS \quad (1)$$

where \dot{X} is the crystal convergence rate (m/s), ρ is the density of the dissolving solid (kg/m^3), J is the solute flux-out of the strip ($\text{kg/m}^2\text{s}$) and S is the effective grain boundary width or mean thickness of fluid in the grain boundary (m). Making use of Fick's law, this leads to:

$$J = \frac{\dot{X}x\rho}{S} = -D \frac{dC}{dx} \quad (2)$$

where C is the solute concentration (kg/m^3) at a given point in the grain boundary fluid, and D is the intrinsic diffusivity of the solute in the grain boundary fluid (m^2/s). Regarding the dissipation balance, solute diffusion at a point in a dilute grain boundary solution produces an energy dissipation rate per unit volume given ($\text{J/m}^3\cdot\text{s}$, Lehner, 1990):

$$\Lambda = -J \frac{d\mu}{dx} \quad (3)$$

where μ is the chemical potential of solute in solution (J/kg). After combining with Equation (2) this yields:

$$\Lambda = D \frac{d\mu}{dC} \left[\frac{dC}{dx} \right]^2 \quad (4)$$

The chemical potential μ is related to the solute concentration C (in kg/m^3 ; Denbigh, 1971) through:

$$\mu = \mu_0 + \frac{RT}{\rho\Omega} \ln \left\{ \frac{C}{C_0} \right\} \quad (5)$$

where μ_0 and C_0 are the solute chemical potential and concentration at equilibrium under unstressed reference

conditions, R is the universal gas constant ($8.314 \text{ J/mol}\cdot\text{K}$), T is the absolute temperature (K), and Ω is the molar volume of the dissolving solid (m^3/mol). For small departures of C from C_0 , we obtain:

$$\frac{d\mu}{dC} = \frac{RT}{C_0\rho\Omega} \quad (6)$$

Moreover, from Equation (2) it follows that:

$$\frac{dC}{dx} = -\frac{\dot{X}x\rho}{DS} \quad (7)$$

Inserting Equations (6) and (7) in Equation (4) thus yields:

$$\Lambda = \frac{RT\rho}{DC_0\Omega} \left[\frac{\dot{X}}{S} \right]^2 x^2 \quad (8)$$

for the pointwise dissipation rate per unit volume within the grain boundary fluid. Accordingly, the dissipation rate Δ_{dx} (in J/s) within a linear strip of width dx within the contact zone is given:

$$\Delta_{dx} = \Lambda \cdot L \cdot S \cdot dx = \frac{LRT\rho}{DC_0\Omega S} \dot{X}^2 x^2 dx \quad (9)$$

We can therefore write for the total dissipation rate in a contact of length L due to solute diffusion out of the contact zone:

$$\Delta_{gb} = 2 \left[\frac{LRT\rho\dot{X}^2}{DC_0\Omega S} \int_{x=0}^{x=+0.5W} x^2 dx \right] \quad (10)$$

yielding:

$$\Delta_{gb} = \frac{LRT\rho\dot{X}^2}{12DC_0\Omega S} W^3 \quad (11)$$

In line with our assumption that all work done by the force applied to the contact is dissipated by diffusion controlled IPS, this must balance the mechanical work rate:

$$\Delta_c = \sigma_n \dot{X}L \cdot W \quad (12)$$

where σ_n is the effective contact normal stress exerted by the dead weight. Thus, since $\Delta_c = \Delta_{gb}$ and $\sigma_n = F/L \cdot W$ we can write the convergence rate as:

$$\dot{X} = \frac{12Z\Omega F}{RT\rho LW^3} \quad (13)$$

where:

$$Z = D \cdot C_0 \cdot S \quad (14)$$

is a kinetic coefficient (kg/s) reflecting the effective grain boundary diffusivity.

1.4 Model B (Diffusion Parallel to the Long Edge of the Contact Interface)

A similar analysis can be made for the case of IPS controlled by the rate of diffusion parallel to the long edge of the contact. The expression for \dot{X} then takes the form:

$$\dot{X} = \frac{12Z\Omega F}{RT\rho L^3 W} \quad (15)$$

Note that the two models A and B differ in the values of the exponents to W and L . In the case of diffusion parallel to the short edge of the contact, the theoretically predicted exponent to W is 3 (Eq. 13), while for diffusion parallel to the long contact edge it is 1 (Eq. 15).

2 EXPERIMENTAL METHOD

The contact dissolution experiments reported here were designed to test if one of the above models describes halite crystal convergence, as well as to observe the contact dissolution process. Four experiments were performed, each involving simultaneous loading of two prism-plate contact assemblies (Fig. 1). Three of the experiments were done using halite-halite assemblies (experiments T1, T2 and T3) whereas one was done using halite-glass assemblies (T4); see Table 1.

2.1 Sample Preparation

The prismatic halite test pieces were prepared by cleaving optical-grade synthetic halite crystals (*Harshaw Chemical Company*) along the (100) crystal planes into parallelepiped-shaped crystals, with long edges of about 5.5 mm and short edges of about 0.7 mm. All crystals were annealed for a

period of 15 to 18 h at 740°C and 1 atm. in an argon gas environment (< 5 ppm H₂O).

In preparing individual experiments, two prismatic crystals were mounted parallel to each other on a glass (thin section) slide using epoxy resin, with the (010) and (100) crystal faces oriented at an angle of 45° (± 5°) to the glass slide (Fig. 1 and Fig. 2a). Smaller halite cubes with edge lengths of about 500 µm were placed in the epoxy to support the prisms (Fig. 2a). After the epoxy had hardened, the sharp upper edges of the two prisms were lightly abraded with 1200-grade SiC polishing paper, and then chemically polished on tissue paper moistened with distilled water. This produced a scratch-free rectangular top surface, subparallel to the (110) plane, with widths in the range 25 to 80 µm (Fig. 2b, and Table 1).

Step 2 of preparing the halite-halite experiments (T1, T2 and T3; Table 1) consisted of fixing two cleaved halite plates or “wafers” (2 mm thick, with edges of 10 mm) to a second glass slide using epoxy resin. The orientation of the halite wafers with respect to the prisms is illustrated in the inset to Figure 3. One wafer was oriented such that one of its (001) directions was parallel to the (001) axis of its “partner” prism (contact Type A). The second was rotated by approximately 45° (contact Type B). The (100) face of the two wafers, ultimately to be pressed against the tilted prisms, was treated in a similar fashion to the edges of the prisms.

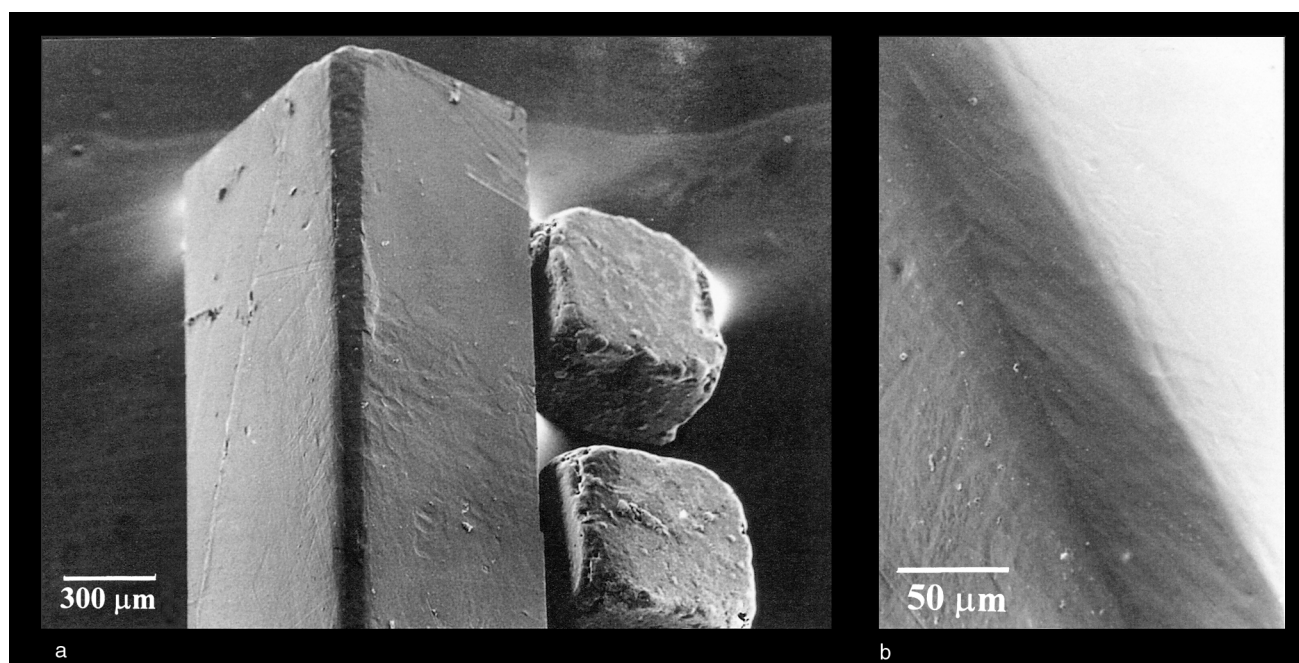


Figure 2

SEM micrographs showing typical prismatic halite single crystal used in the contact dissolution tests. Note support by smaller halite crystals (a). After abrasion with fine polishing paper, the top face was chemically polished with a tissue moistened with distilled water to produce a smooth scratch-free top surface (b).

TABLE I
Experimental Data

Test	Contact type	Time period (days)	Load (σ) at time period	Contact force (N) over given time period (τ)	Contact width measurements			Contact normal stress values			Crystal convergence rates								
					Locations on crystal A where (w) measured	Locations on crystal B where (w) measured	Number of measurements of (w) per location	Minimum average value of (w) at crystal A	Maximum average value of (w) at crystal A	Minimum average value of (w) at crystal B	Maximum average value of (w) at crystal B	Minimum contact normal stress (MPa) at crystal A	Maximum contact normal stress (MPa) at crystal A	Minimum contact normal stress (MPa) at crystal B	Maximum contact normal stress (MPa) at crystal B	Minimum convergence rate crystal A ($\times 10E-11$ m/s)	Maximum convergence rate crystal A ($\times 10E-11$ m/s)	Minimum convergence rate crystal B ($\times 10E-11$ m/s)	Maximum convergence rate crystal B ($\times 10E-11$ m/s)
T1	Halite-halite	0 to 0.5	208	1.0	1	4	1	40	84	53	66	4.6	2.2	3.5	2.8	(****)	-	-	-
		0.5 to 10	324	1.6	1	4	5	84	150	66	113	3.4	1.9	4.4	2.6	20	1	6.3	0.3
		10 to 19	549	2.7	1	4	2	150	158	113	154	3.3	3.1	4.3	3.2	(****)	-	-	-
T2	Halite-halite	0 to 25	208	1.0	5	3	25	85	43	106	7.4	2.2	4.3	1.7	8.4	0.3	7.6	0.1	
		25 to 27	373	1.8	5	3	78	85	106	106	4.3	3.9	3.1	3.1	(****)	-	-	-	
T3	Halite-halite	0 to 61	208	1.0	(**)	(***)	63	233	63	233	2.9	0.8	2.9	0.8	(****)	-	-	-	
T4	Halite-glass	0 to 8	208	1.0	2	3	n.m.	131	n.m.	193	-	1.4	-	1.0	(****)	-	-	-	
		8 to 25	368	1.8	2	3	137	164	211	254	2.4	2.0	1.6	1.3	0.6	0.4	3.9	1.2	
		25 to 32	538	2.6	2	3	164	220	248	294	2.9	2.2	1.9	1.6	16	(****)	5.5	5.3	

Notes

- (*) = Taken as the force exerted by the "dead weight" divided by two, taking equal transmission of load to crystal contacts A and B.
- (**) = No contact width measurements were made during the experiment, but average contact width was measured before and after the experiment on crystal A.
- (***) = Not measured; Contact surface area of crystal B assumed to be the same as that of crystal A for calculation of contact stress
- (****) = Not measured
- (*****) = Only one convergence rate obtained

In the halite-glass experiment reported in this paper (T4, Table 1), the prismatic halite crystals were loaded directly against an overlying glass slide.

The complete sample preparation procedure was carried out in a dry room (relative humidity $RH < 20\%$) to minimize any influence of atmospheric water on the surfaces of the halite crystals. Prior to experimentation the samples were sealed in plastic boxes containing silicagel, and stored in the dry room.

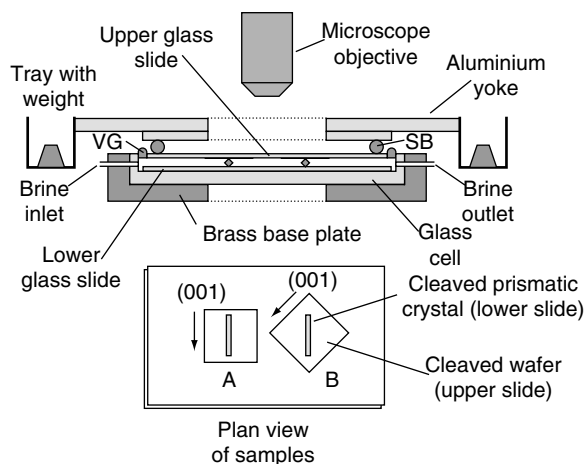


Figure 3

Schematic diagram of the apparatus used in this study to exert a constant force normal to halite-halite and halite-glass contacts, while viewing them through an optical microscope; VG = vacuum grease, SB = cylindrical steel bearing. In the inset showing the plan view of the samples, note orientation of the two halite wafers, fixed to the top slide, with respect to the tilted prismatic crystals, fixed to the bottom slide (tests T1-T3): contact Type A = tilted contact, contact Type B = tilted + twisted contact.

2.2 Loading Apparatus and Testing Procedure

The loading apparatus used in the contact dissolution experiments and its positioning under the optical microscope are illustrated in Figure 3. The lower glass slide with its two prismatic crystals, and the upper glass slide with (T1-T3) or without (T4) halite wafers, are positioned as shown. The open rim between the glass cell walls and the top slide are sealed with low-viscosity Dow Corning vacuum grease. Normal force F is applied to the crystal contacts using the weight of the aluminium yoke (mass 208 g, length ≈ 15 cm; Fig. 3). The load can be increased by placing equal weights in small trays fixed on opposite sides of the yoke. The total weight of the yoke is transmitted to the crystals *via* two cylindrical steel bearings (diameter 3 mm) resting on the top glass slide. Yoke, bearings and halite crystals are placed symmetrically (Fig. 3). Furthermore, the separation of the

two prismatic crystals is a factor of about 200 larger than the average contact width W . It can therefore be safely assumed that equal contact forces F , equal to half the dead weight force, act on the two crystal contacts during each experiment. Note that the transmitted light beam is orthogonal to the crystal contacts, thus allowing direct observations to be made of the contact microstructure as well as stepwise measurement of the contact width W .

All tests were conducted in the presence of brine saturated with respect to NaCl at room temperature. In each experiment, the brine was injected after assembly of the cell, but before application of the load. Injection of brine into the glass cell at a rate of about $0.5 \mu\text{l/s}$ expelled nearly all of the air from the cell through the outlet port (Fig. 3). Immediately upon addition of the brine, the contact interface developed a conspicuous transparency allowing inspection of contact features to an optical resolution of about $1 \mu\text{m}$. After filling the cell with brine, the inlet was plugged and the outlet sealed with a latex membrane. The cell was finally weighed and mounted on the optical microscope stage.

Normal load was subsequently applied to the crystal contacts by carefully placing the aluminium yoke and steel bearings in position on the top glass slide. Depending on the initial surface area of the two contacts A and B, initial mean normal stresses on the contacts fell in the range 2.9 to 7.4 MPa. In T1, T2 and T4, additional contact load was applied during the course of the experiment by placing equal weights simultaneously on both sides of the yoke. Table 1 lists the load and stress path for all four experiments. In all tests, the applied contact stress fell in the range 2 to 5 MPa during most of the test duration.

At regular time intervals, contact width measurements were made at different locations along the long edge of the contact, using a calibrated graticule ($\pm 3 \mu\text{m}$ estimated accuracy). The first width measurements were made a few minutes before application of the load and again several minutes after loading. Subsequent measurements were made every few days. Table 1 lists the number of contact width measurements that were made at each location. Periodically, overview and high-magnification photomicrographs were taken of the contact microstructure, using transmitted light.

The values of W measured at the different locations showed a considerable variation. This is thought to be partly due to deviations from a perfectly rectangular contact shape, and partly due to errors in retracing the locations where W was to be measured (estimated to be within $\pm 10 \mu\text{m}$). Where average values of W are presented graphically, an "error bar" will be shown, representing the spread (range) of all measurements of W along the relevant contact at a given time. The standard deviation about the arithmetic mean of W , measured at a given contact at a given time, ranged from 6 to $24 \mu\text{m}$ in T1 (average $16 \mu\text{m}$) and from 6 to $15 \mu\text{m}$ in T2 (average $8 \mu\text{m}$).

2.3 Test Termination

Experiments were terminated by carefully lifting the yoke from the cell. The cell was then removed from the microscope stage and quickly weighed to check for evaporation of water from the brine (never significant). The top and bottom glass slides were subsequently extracted, and the halite crystals immediately rinsed in hexane to remove any brine. Residual hexane was removed using absorbent tissue paper. The dried halite crystals were subsequently stored in the low-humidity room and prepared for further microstructural analysis using optical and scanning electron microscopy (SEM). Note that sample extraction according to the above procedure took only 30 to 40 seconds, and that the “wet” halite crystals were exposed to the atmosphere for only 5 to 10 seconds. Pilot tests revealed that, over this time span, no optically visible NaCl-precipitate formed from brine droplets residing on the surface of the halite crystals.

3 CONTACT WIDTH DATA

3.1 Halite-Halite Contacts (Experiments T1, T2 and T3)

In the halite-halite experiments, no change in contact width W was measured between the readings taken a few minutes before and after loading. However, a gradual increase of average contact width was recorded as a function of time in the ensuing days, at a rate which tended to decrease with time for a fixed load. This is illustrated in Figures 4 and 5 for experiments T1 and T2. Note that no convergence data were collected in T3. In the first stage of experiment T1, it can be seen from Figure 4 that larger values of W were achieved at crystal contact A (tilt only) than at contact B (tilt + twist). In the first stage of experiment T2, however, larger values of W were achieved at crystal B (tilt + twist) than at crystal A (tilt only). In stage 2 of experiment T1, a contact force of 1.6 N was applied between day 1 and day 10 (Table 1). Increasing the contact force from 1.6 to 2.7 N at day 10 produced an increase in W at crystal contact B of a few tens of micrometres over a time period of 3 days (Fig. 4b). No such increase occurred at crystal A (Fig. 4a). However, increasing the contact force from 1.0 to 1.8 N at day 25 in T2 led to a reduction in W of up to 10 μm at crystal contact A within a few hours (Fig. 5a), while contact B showed no measurable contact width change (Fig. 5b). No further contact width measurements were made in T2 after day 25.

3.2 Halite-Glass Contacts (Experiment T4)

Figure 6 shows the average contact width W as a function of time and load in the halite-glass experiment T4, for crystals A (Fig. 6a) and B (Fig. 6b). No contact width

measurements were made from day 1 to 8, when the initial applied contact force was 1.0 N. Straight line segments connect the average values of W determined over the two subsequent periods of constant contact forces of 1.8 N (day 8 to 25, bold line) and 2.6 N (day 25 to 32, dashed line); see also Table 1. There is an increase in W with time in the second phase of the experiment (day 8 to 25, 1.8 N) at both contacts A and B. In the third phase (day 25 to 32, 2.6 N), however, the data show contradictory behavior. Crystal A showed a strong increase in W followed by a slight decrease in W (Fig. 6a). Crystal B initially showed no contact widening nor even a slight contact area reduction, but from day 27 to 32 the widening rate was roughly constant (Fig. 6b).

4 CONVERGENCE RATE DATA

No evidence was found for significant marginal dissolution effects or preferential precipitation near individual contacts (see below). Therefore, convergence rates \dot{X} could be justifiably calculated from the heavy straight line segments shown in Figures 5 and 6 between data points (W values) obtained at constant load using the relation $\dot{X} = \dot{W}/2$, where \dot{W} is the rate at which the contact width increased over time. For all tests, \dot{W} data were obtained from the slope of these straight line segments (Figs. 4 to 7) and are hereafter plotted as a function of the corresponding midpoint contact width W .

4.1 Halite-Halite Contacts (Experiments T1, T2 and T3)

Figure 7a shows the logarithm of \dot{X} as a function of the logarithm of W , obtained for crystal contacts A and B from experiment T1 at a contact force of 1.6 N. Values for \dot{X} range from 2×10^{-10} m/s to 3×10^{-12} m/s, with values of W in the range 60 to 160 μm . For contact A, \dot{X} decreases with increasing W . Assuming a power law relationship $\dot{X} \propto W^n$ to describe the data, in accordance with the theoretical models for diffusion-controlled IPS, the exponent n to W is about -5 for crystal A. The data obtained for crystal B indicate an increase and then an overall decrease in \dot{X} with increasing W . Note that, at any given W , \dot{X} is higher at crystal contact A than at crystal B.

Figure 7b shows the log of \dot{X} as a function of log W , measured for crystal contacts A and B in experiment T2 at a contact force of 1.0 N. Values for \dot{X} range from 8×10^{-11} m/s to 8×10^{-13} m/s, with values of W in the range 40 to 110 μm . Clearly, the variability in \dot{X} at almost constant W is large (up to a factor of 20). However, the trend in the data also indicates a decrease in \dot{X} with increasing W , with an exponent (n) to W in the range -3 to -5 , assuming a power law relationship. At any given W , \dot{X} is usually higher at crystal B than at A. Since W was not measured for T3, no \dot{W} data are available for this experiment.

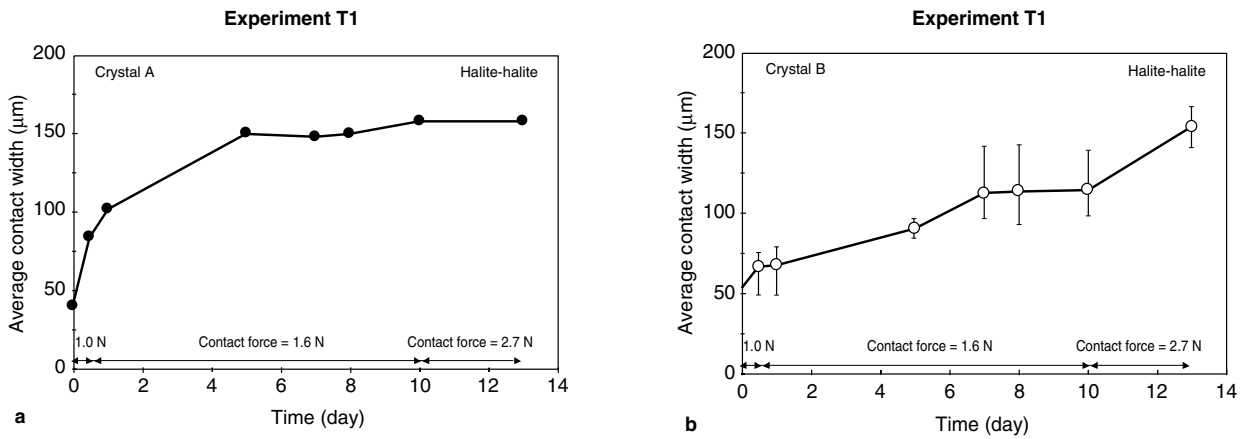


Figure 4 Average contact width (W) as a function of time measured in halite-halite contact experiment T1 at crystal contact A (a) and crystal contact B (b). The bold line segments were used to calculate the crystal convergence rate at a constant contact force of 1.6 N.

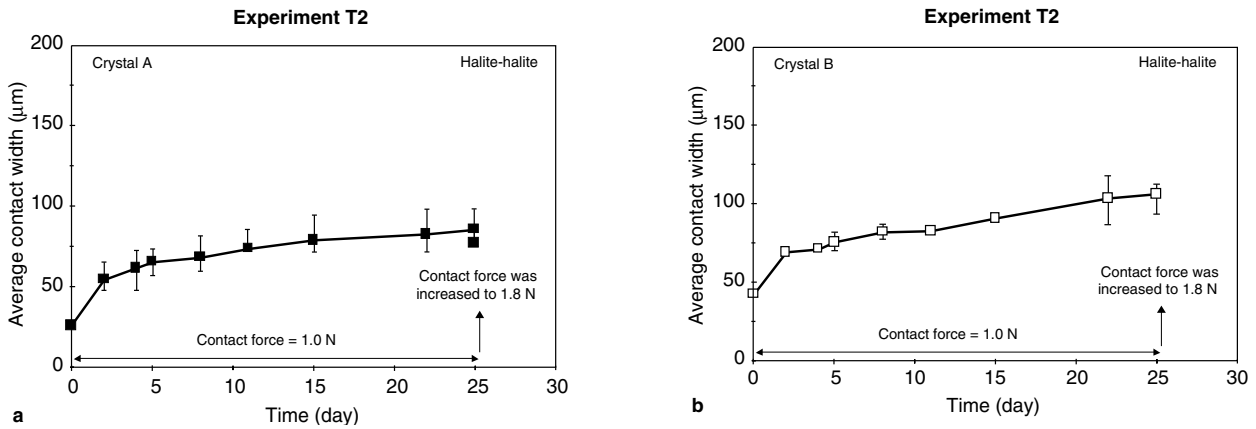


Figure 5 Average contact width (W) as a function of time measured in halite-halite contact experiment T2 at crystal contact A (a) and at crystal contact B (b). The bold line segments were used to calculate the crystal convergence rate at a constant contact force of 1.0 N.

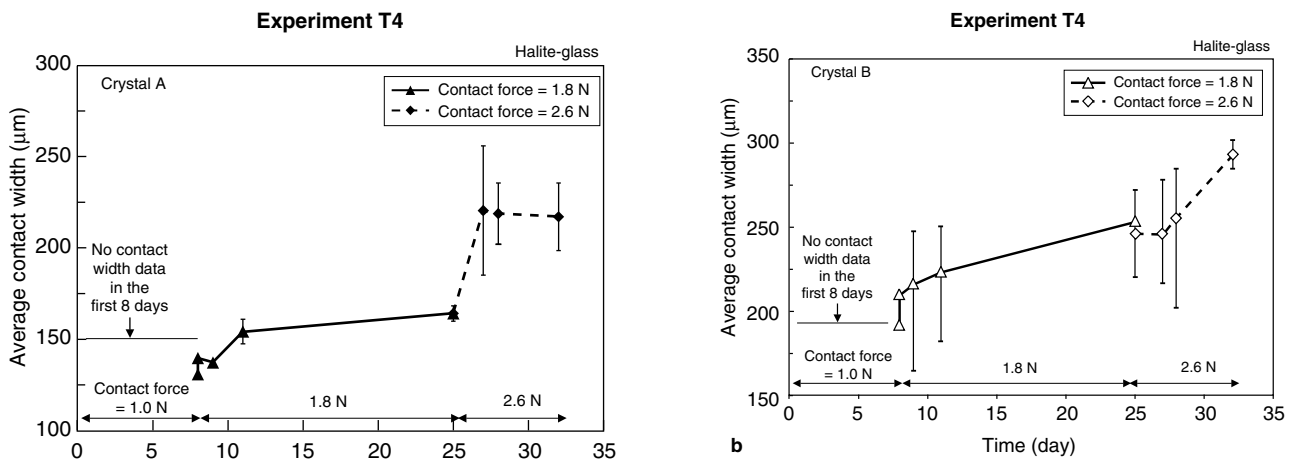


Figure 6 Average contact width (W) as a function of time measured in halite-glass contact experiment T4 on crystal A (a) and contact B (b). No mechanical data were collected in the first 8 days.

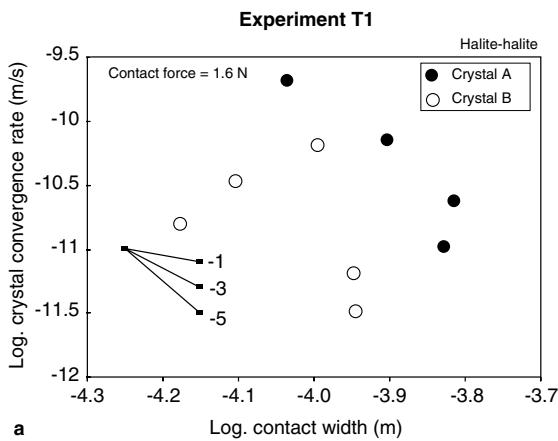


Figure 7a

Logarithm of the crystal convergence rate \dot{X} as a function of the logarithm of average contact width W measured at crystal contacts A and B in halite-halite contact experiment T1. \dot{X} was obtained from data shown in Figures 4a and 4b.

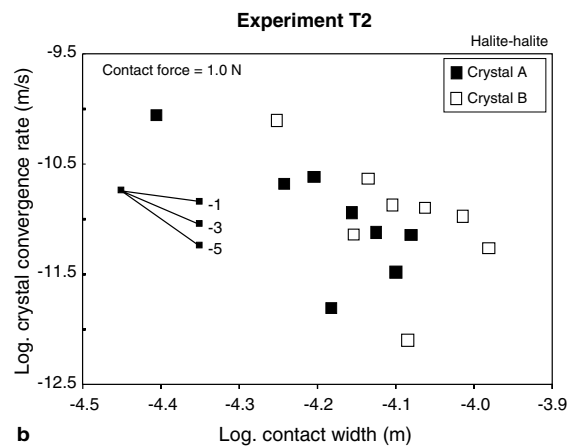


Figure 7b

Logarithm of \dot{X} as a function of the logarithm of W measured at crystal contacts A and B in halite-halite contact experiment T2. \dot{X} was obtained from data shown in Figures 5a and 5b.

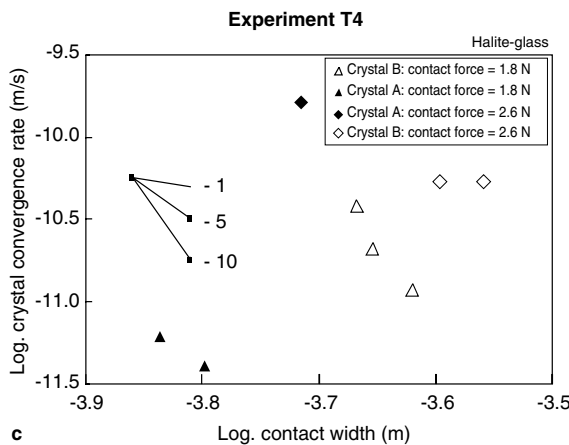


Figure 7c

Logarithm of \dot{X} as a function of the logarithm of W measured at crystal contacts A and B in halite-glass contact experiment T4. \dot{X} was obtained from data shown in Figures 6a and 6b.

4.2 Halite-Glass Contacts (Experiment T4)

Figure 7c shows the logarithm of \dot{X} as a function of the logarithm of W measured in halite-glass contact experiment T4. Values for \dot{X} at a constant contact force of 1.8 N are indicated by triangles, and values for \dot{X} , obtained after an increase of contact force to 2.6 N, by rhombs. The data obtained at the lowest contact force of 1.8 N show that \dot{X} decreases with increasing W , as seen in the halite-halite experiments. The few data indicate a strong dependence of \dot{X} on W . Increasing the contact force from 1.8 to 2.6 N led to an increase in \dot{X} by a factor of 40 at crystal contact A (from 4×10^{-12} m/s to 1.6×10^{-10} m/s) and by a factor of 5 at crystal B (from $\sim 10^{-11}$ m/s to 5×10^{-11} m/s).

5 MICROSTRUCTURAL OBSERVATIONS

5.1 Observations on Addition of Brine and Emplacement of Yoke

As already mentioned, immediately upon addition of the brine, the halite crystals appeared more transparent than when dry, and the contact interface developed a conspicuous transparency allowing inspection of contact features to an optical resolution of about $1 \mu\text{m}$. This change in appearance (“transparency”) of the contacts upon addition of brine demonstrated that the brine initially wetted the (unloaded) halite/glass and halite/halite contacts. No morphological

changes were observed in the ensuing minutes before application of the load.

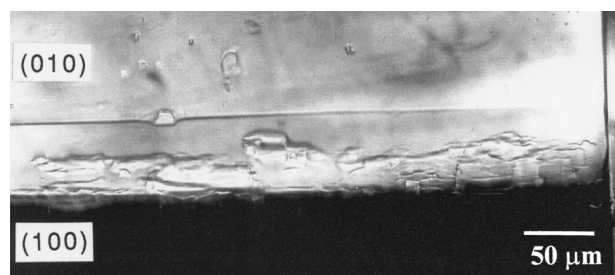
During and shortly after emplacement of the yoke, no systematic observations were made of the contact morphology. After several minutes, however, it was noted that a roughness or “scar” structure had developed on the scale of several tens of micrometres, though no change in W was yet apparent. The initial roughness evolved within two to five hours into a smoother contact, with progressive development of optically flat regions within the gradually widening contact. Nevertheless, after 0.5 day at a contact load of 0.5 N, the bottom half of the contact of crystal A in test T1 still showed remnants of the initial roughness (Fig. 8a). The upper (photograph view) part of the contact has turned optically smooth; the lower part shows roughness that formed during or shortly after emplacement of the yoke.

5.2 Effects of Load Change and Time on Contact Structure

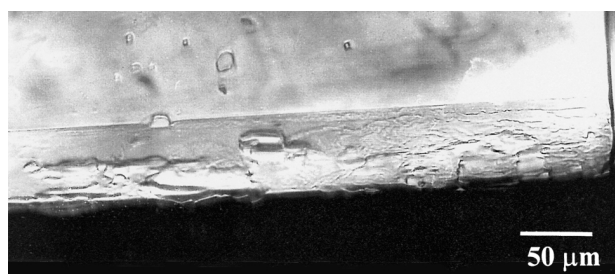
Figure 8(a-c) illustrates the effect of an instantaneous increase in load on the halite-halite contact morphology at crystal contact A in T1. The contact morphology just before the stress increment is shown in Figure 8a. As indicated above, it has been loaded under brine by the weight of the yoke (1.0 N per contact) for a period of 0.5 day. Micrographs 8b and 8c are taken 1 min and 4 min after increasing the applied load from 1.0 to 1.6 N, corresponding to an increase in average normal stress at contact A from 2.2 to 3.4 MPa (Table 1, Fig. 4a). Numerous small crystal ledges and channels or grooves appear in the smooth part of the halite/halite contact within 20 to 60 s after the stress increment (Fig. 8b). Within a few minutes, the contact relief has considerably increased in amplitude (Fig. 8c) with simultaneous development of an interconnected network of “islands and channels”, several micrometres wide. Most of these are oriented subparallel to the long edge of the contact face, i.e. along the (001) crystallographic direction. The entire contact now shows a surface roughness. This did not appear to migrate from the rough zones into the smooth regions, but rather formed *in situ* within the smooth regions. No evidence of marginal dissolution or of significant contact widening was observed during the roughening event.

Over periods of several days, the above type of stress-increment-induced, rough contact microstructure, evolved to an optically smooth contact morphology, enclosing characteristic oval to elongate inclusions, their long dimension always parallel to the long edge of the contact face. The length of the inclusions ranged from a few to 50 μm , and their aspect ratio at the contact face was typically 1:10, though ratios of 1:2 to 1:5 were also common. Figure 9a-c shows a typical sequence of observations of the top face of halite-halite contact A in T3 (contact surface of lower prismatic crystal), taken after 3, 14 and 35 days, respectively, under a

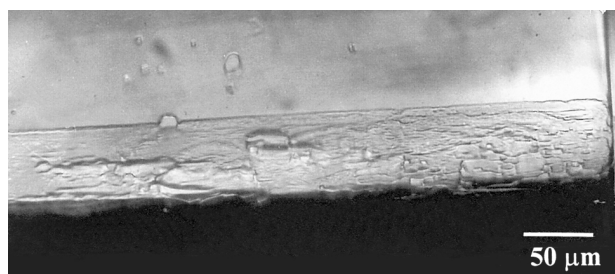
constant applied load of 1.0 N, exerting a normal stress which gradually decreased from 2.9 to 0.8 MPa over two months (Table 1). Note the time-dependent change in shape and the decrease in size of grooves and inclusions, the ultimate disappearance of the smaller inclusions and the gradual increase in contact width.



a



b



c

Figure 8

Series of micrographs showing the “contact roughening” process at the halite-halite contact A in experiment T1. a: contact microstructure after 0.5 day at a contact force of 1.0 N. Top part of the contact surface area is optically smooth, while bottom part is covered with elongate grooves (“scars”). These are remnants of roughness formed during or after emplacement of the yoke.

b: fine-scale (“mottled”) roughness of the upper part of the contact appearing 1 min after increasing the load from 1.0 to 1.6 N.

c: micrograph of same area 4 min after increasing the contact force from 1.0 to 1.6 N, showing the evolution towards a characteristic rough contact morphology composed of a crystallographically controlled pattern of “islands and channels”. Note that the new roughness extends over the entire contact.

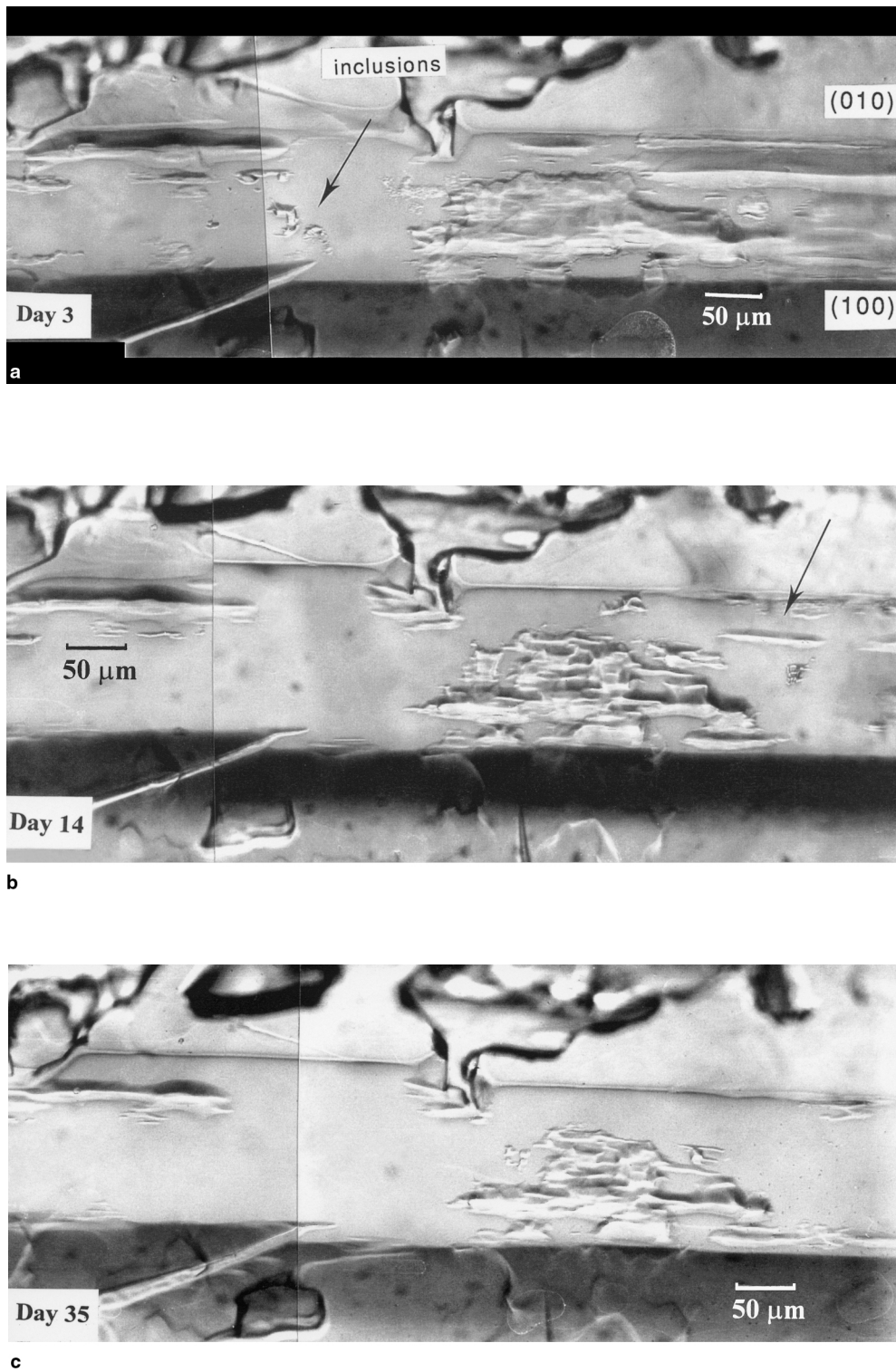
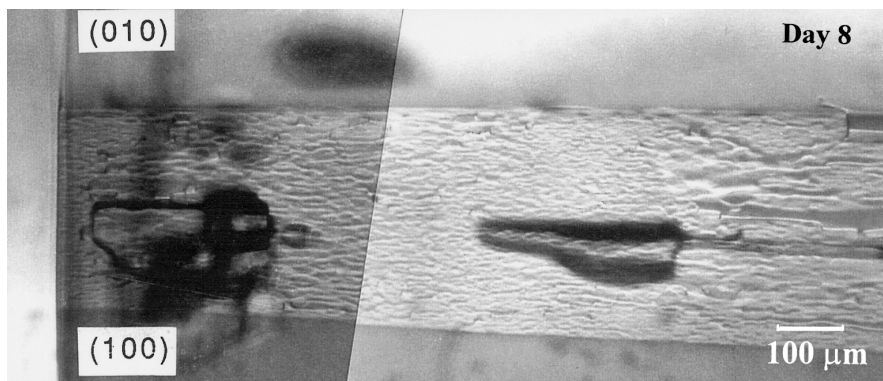
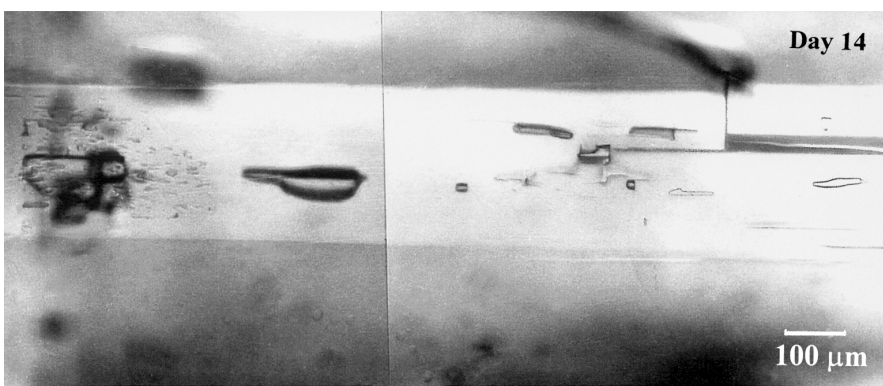


Figure 9

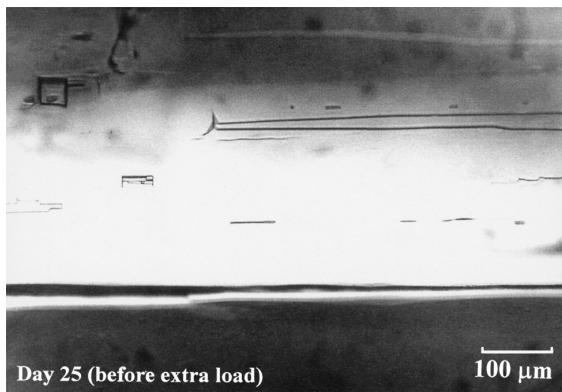
Sequence of optical microscope observations of the contact surface of the prismatic halite crystal A in T3 taken after respectively 3, 14 and 35 days under a constant contact force of 1.0 N, exerting a contact normal stress which gradually decreased from 2.9 to 0.8 MPa over a time period of two months (Table 1). Note that the inclusions decrease in size with time and eventually disappear (see arrows). Note also the relatively bright "optically flat" contact surface regions.



a



b



c



d

Figure 10

Series of optical micrographs showing the effect of applied force and time on the contact morphology of halite-glass contact B in experiment T4. An instantaneous rise in contact force from 1.0 to 1.8 N at day 8 gave the rough contact surface relief shown in Figure 10a (refer to Table 1). Note the crystallographic control on contact morphology development; almost all channels are oriented along (001). With time the surface roughness decreased (Fig. 10b, taken 6 days after the contact force increase), and after 17 days at constant contact force an optically smooth contact surface had formed (Fig. 10c). A renewed increase in contact force from 1.8 to 2.6 N at day 25 triggered the formation of a rough contact surface, with a similar morphology to that observed after the first load increase (Fig. 10a, Fig. 10d).

In the halite-glass experiment (T4), similar observations were made as in the halite-halite experiments. These observations are illustrated in Figure 10 with a series of micrographs showing the effect of contact force and time on the morphology of a halite-glass contact. The contact was first loaded for 8 days by the weight of the yoke (1.0 N contact force). No contact width data were collected and no microstructural observations were made during this period. An instantaneous increase in contact force from 1.0 to 1.8 N at day 8 gave the rough contact surface relief shown in Fig. 10a. Almost all channels are oriented along (001), indicating crystallographic control on contact morphology development. With time and on-going contact widening, the surface roughness steadily decreased (Fig. 10b, taken 6 days after the contact force increase), and after 17 days at constant contact force an optically smooth contact surface had formed (Fig. 10c) surrounding just a few crystallographically controlled inclusions. A renewed increase in contact force from 1.8 to 2.6 N at day 25 triggered the reformation of a rough contact surface, with similar morphology to that observed after the preceding load increment (compare Fig. 10d with Fig. 10a). During the experiment, no evidence was seen for the operation of marginal dissolution (contact undercutting), plastic deformation or microgranulation at the surface of the prismatic halite crystals.

5.3 Further Optical Observations

No observations were made of the contact microstructure during removal of the load (by lifting the yoke) or treatment with hexane to remove residual brine from the crystal surfaces. However, optical examination after the experiments showed that in all experiments removal of material was essentially restricted to the lower tilted prismatic crystal, with little or no mass removal from the upper crystal wafers (experiments T1-T3) or glass plate (T4). Post-test inspection of the crystals under the binocular microscope confirmed the *in situ* observations: no evidence was found for systematic dissolution or undercutting from the edges of the contact (i.e., for the formation of marginal dissolution microstructures), for plastic deformation or for microgranulation at the contacts. In addition, the orientation of the halite wafers used in T1-T3 (tilt only, or tilt + twist; Fig. 3) did not appear to influence contact morphology development, or the rate at which this morphology changed in response to a change in contact stress.

5.4 SEM Observations

Figure 11 shows secondary electron micrographs of the contact microstructure developed on crystal A of experiment T3 after being loaded for two months at a contact force of 1.0 N (contact stress gradually decreasing from 2.9 to 0.8 MPa due to contact widening). Clearly recognizable are

the wedge-shaped grooves running parallel to (001) which correspond to the oval-shaped inclusions visible under the optical microscope (e.g. Figs. 9c and 10c). The intervening regions between the large inclusions show smaller elongate inclusions, a few micrometres in length, that form a surface relief with transverse amplitude and wavelength of a few hundred nanometers (Figs. 11a-d). Some parts of the intervening regions appear to be flat, i.e. any surface relief is irresolvable (< 50 nm). Figures 11b and 11c display both the “rough” and “smooth” contact morphology, and the transition between them, as well as a characteristic braided pattern of channels, a few micrometres wide/deep and several tens of micrometres long. The average thickness of the halite/halite contact zone for crystal A in experiment T3 (i.e., including the large oval inclusions and the smaller relief) is estimated to be a few hundred nanometers.

6 DISCUSSION

6.1 Processes Active at the Crystal Contacts

The present results have shown that prismatic halite crystals loaded edgewise (i.e. in the (110) direction) against the face of a cleaved (100) halite wafer or against a glass plate, in the presence of saturated brine, undergo time-dependent removal of material from the contact interface, at normal stresses in the range 1 to 7 MPa. As evidenced by the increase in contact transparency when the brine was initially added, all contacts were penetrated by brine before loading. Recall that no morphological changes were observed at that stage. However, when load was first applied, all contacts showed rapid and pervasive roughening of the “wetted” contact surface. Since the first few minutes of the process were not observed, it may have involved either internal contact roughening or localised marginal dissolution, presumably triggered by free-energy increases related to elastic and/or plastic deformation at the lower crystal contact.

Our results further show that the initial loading/roughening stage was followed by on-going, decelerating convergence accompanied by a gradual smoothing of the rough grain boundary (island-channel type) structure towards an optically flat configuration surrounding residual brine-filled channels and inclusions which continued to decrease in size with time. In all experiments, convergence continued even after the optically smooth contact structure was established (e.g. T3, Fig. 9). The convergence/smoothing process must therefore have involved diffusion of mass out of the contact, and expulsion of inclusion-trapped brine, through a connected brine phase present within grain contacts. When contact stresses were increased, the optically smooth contact structure reroughened within minutes (Fig. 8), presumably due to inhomogeneous plastic and/or elastic deformation, and

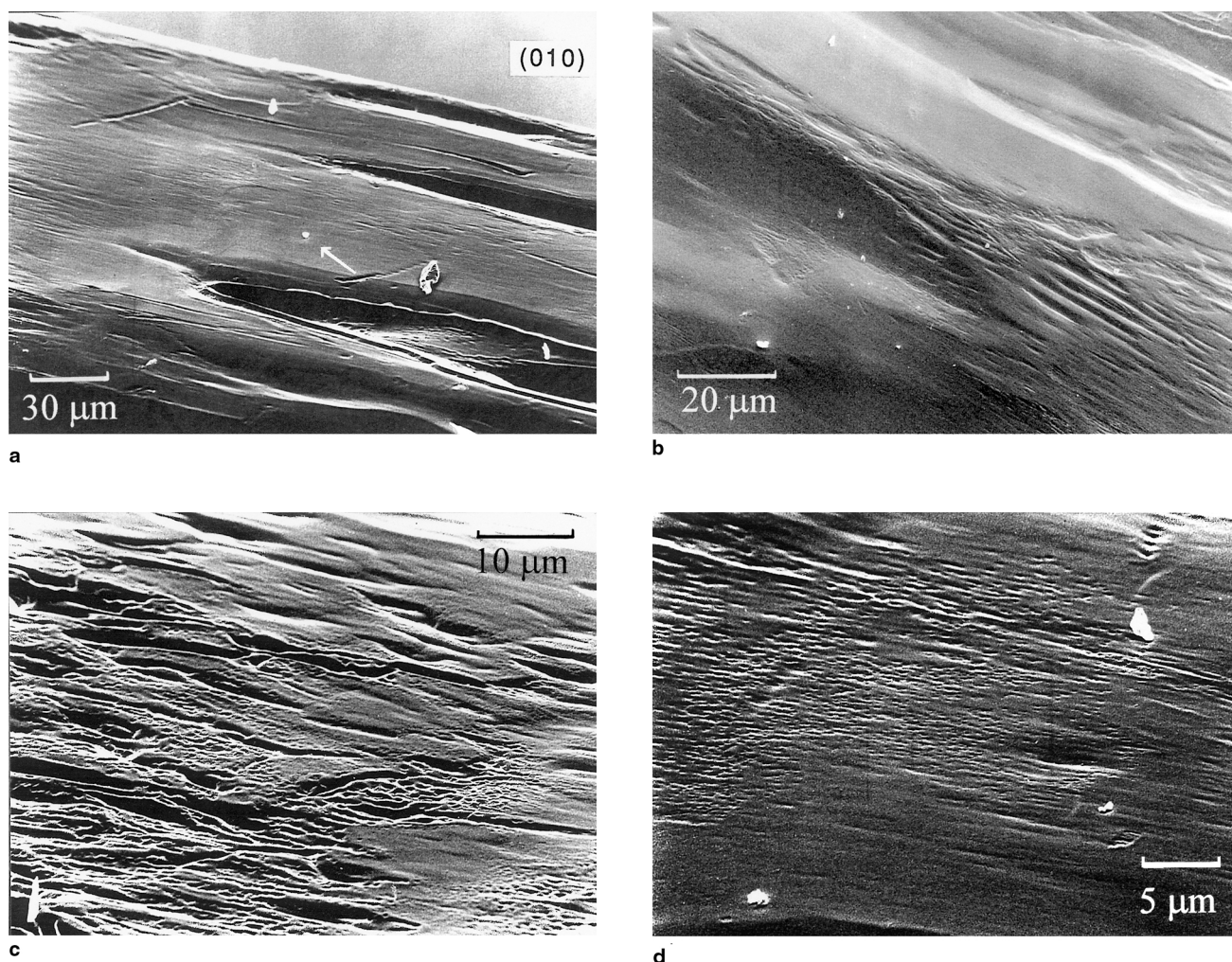


Figure 11

SEM photomicrographs of contact surface of prismatic halite crystal loaded against a halite wafer for 61 days in experiment T3 (contact A). All four micrographs are taken at an angle of approximately 45° to the contact surface area. The surface roughness is made up of a pattern of elongate islands and channels, separated by zones with no visible surface relief (a and b). This pattern of rough and smooth regions occurs at all resolvable scales. Even at submicron scales a roughness occurs with an estimated island-channel amplitude-wavelength of a few 100 nm (c and d).

the cycle of time-dependent convergence and gradual smoothing out of the contact structure repeated itself. Only in one experiment (T2, contact A) did the contact width decrease on reloading, suggesting some form of marginal dissolution.

Putting all of our observations together, we infer that after initial loading, when marginal dissolution may have occurred, the convergence observed in our experiments took place by some kind of stress- or strain energy driven grain boundary diffusional IPS mechanism. This involved diffusive mass transport through wetted contacts characterized by an island-channel type structure, the amplitude of which appears to depend on normal stress and time, increasing shortly after

increasing the stress and decreasing to optical flatness with on-going convergence at constant load.

The rough contact structure observed optically during the experiments is clearly a nonequilibrium feature and closely resembles that preserved in our previous compaction experiments on wet granular salt (Spiers and Schutjens, 1990; Spiers *et al.*, 1990; Spiers and Brzesowsky, 1993) and proposed in various models for grain boundary diffusional IPS (Lehner, 1990; see also Tada *et al.*, 1987). Whether a fine-scale rough structure persisted in contacts which evolved to optical flatness is not known, though our post-experimental SEM observations suggest that it may have. If so, its amplitude was certainly less than $1\ \mu\text{m}$ (optical

resolution), and probably even less than 500 nm. If not, then a thin brine film must have existed in such contacts to allow the observed on-going convergence and elimination of isolated brine inclusions. Such films could potentially be maintained either by surface forces (adsorbed film) or even hydrodynamic forces. Such a film could also have separated solid contact points within the optically visible island-channel structure.

Lastly we note that from the present halite-halite contact experiments no consistent effect of prism-wafer twist on convergence behavior can be deduced. Regarding the halite-glass contacts, these seem to show somewhat faster convergence rates than the halite-halite contacts, taking into account the contact widths (Fig. 7). This may indicate some effect of the glass on contact fluid thickness or properties (cf. findings of Hickman and Evans, 1991, 1992, 1995), though the data are too few to conclude this firmly.

6.2 Comparison with Model

On the basis of the above observations, it seems justified to compare our results with the predictions of our theoretical models for stress-driven, grain boundary diffusion-controlled IPS, in an attempt to assess how far the models can account for the experimental observations. Figure 12 shows a compilation of all convergence rate data obtained in the present study. It consists of a log-log plot of force-normalized convergence rate (\dot{X}/F) versus contact width W . According to our models, which are derived assuming constant effective grain boundary diffusivity Z , all (\dot{X}/F) versus W data thus plotted should cluster about a single straight line with a slope of -3 (Model A, Equation 13, diffusion parallel to the contact width W) or of -1 (Model B, Equation 15, diffusion parallel to the contact length L). Clearly, this is not the case—the data are widely scattered. Nonetheless, from Figures 7a-c and Figure 12 it is evident that individual contacts subjected to a fixed force show a systematic tendency for the quantity (\dot{X}/F) to decrease with increasing W . Focussing on the data for individual halite-halite contacts in Figure 12, and assuming a power law relationship $\dot{X}/F \propto W^n$, a linear least squares fit to the data yields values for n ranging from -2.2 (T1, crystal B) to -5.2 (T1, crystal A), with an average value of n of -3.75 , though the correlation coefficients are low. Note also that, at a given value of W , values of \dot{X}/F obtained in T1 are about an order of magnitude higher than values for \dot{X}/F obtained in T2. Similarly, fits made to the halite-glass contact data yield n -values of -4.6 (experiment T4, A, 1.8 N) and -10.2 (experiment T4, B, 2.6 N). The observed n -values are thus inconsistent with diffusion occurring along the long edge of crystal contacts as described by our Model B (theoretical exponent n of -1 ; see Eq. 15).

We propose that a more likely explanation for the observed behavior is that convergence at individual contacts

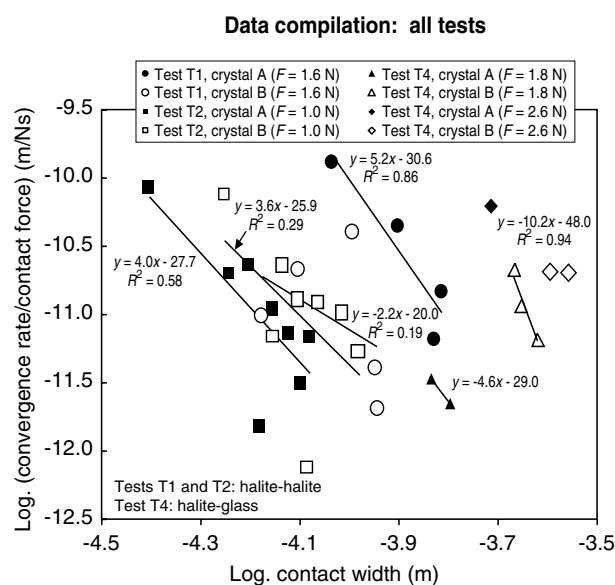


Figure 12

Compilation of all crystal convergence rate data as a function of contact width. Note that the convergence rate (\dot{X}) is normalised with respect to the contact force (F). Assuming a power law relationship $\dot{X}/F \propto W^n$, linear least squares fits have been added to individual contact data sets as shown.

Note that the data for halite-halite contacts yield values for n ranging from -2.2 (T1, crystal B) to -5.2 (T1, crystal A). Note also that, at a given value of W , values of \dot{X}/F at T1 are about an order of magnitude higher than values for \dot{X}/F obtained at T2. The limited data for halite-glass contacts indicates n -values of -4.6 (T4, contact A, $F = 1.8$ N) and -10.2 (T4, contact B, $F = 1.8$ N).

was controlled by diffusion parallel to the contact width W in a manner similar to that described by Model A ($n = -3$), but with the effective grain contact diffusion coefficient ($Z = D \cdot C_0 \cdot S$) and perhaps also path length being influenced by:

- variations in grain contact structure (roughness) from contact to contact;
- variations in contact structure caused by variation in applied force, and
- a tendency for the grain boundary thickness S to decrease with on-going convergence at constant force.

This interpretation is consistent with our observations that some crystal contacts (e.g. T1, contact A) were much rougher than others (e.g. T1, contact B), that all contacts became smoother with time at constant applied load, and that the n -values implied by the fits presented in Figure 12 are mostly larger than 3 in magnitude (the value expected from Model A if Z is a constant—see Eq. 13). The proposed interpretation thus accounts for most of our experimental observations.

In the framework of this interpretation, let us compare our results directly with Model A (Eq. 13) in an attempt to

estimate bounds for Z which can be compared with values calculated from our previous compaction experiments on wet granular salt (Spiers and Schutjens, 1990; Spiers *et al.*, 1990; Spiers and Brzesowsky, 1993) in which grain boundary diffusion was inferred to control the rate of IPS. To do this, we make use of the (\dot{X}/F) versus W relations for the halite-halite contacts represented by the least squares fits to the data presented for T1 and T2 in Figure 12. For each contact (T1 A, B and T2 A, B), the kinetic coefficient (Z) can then be obtained as a function of W by rewriting Equation (13) in the form:

$$Z = DC_0S = \frac{RT\rho LW^3}{12\Omega} \frac{\dot{X}}{F} \quad (16)$$

and taking $R = 8.314 \text{ J/mol}^\circ\text{K}$, $T = 293^\circ\text{K}$, $\rho = 2165 \text{ kg/m}^3$, $L = 5.5 \times 10^{-3} \text{ m}$ and $\Omega = 2.693 \times 10^{-5} \text{ m}^3/\text{mol}$. We restrict attention to the halite-halite contacts since very few data were obtained from the halite-glass experiment (T4).

Figure 13 shows Z as a function of W as calculated from Equation (16) using the upper and lower bound best fit relations between (\dot{X}/F) and W obtained from Figure 12 for the halite-halite contacts (T1, A and T2, A respectively). The curves shown in Figure 13 thus reflect the spread in Z implied by our experimental data, assuming that our interpretation of a Model A type mechanism of IPS is correct. The range in values of Z obtained is from $4 \times 10^{-16} \text{ kg/s}$ to $4 \times 10^{-14} \text{ kg/s}$ for contact widths in the range 50 to 175 μm . Note that the curves presented in Figure 13 show a decrease in Z with increasing W . The lower bound values for Z obtained in the analysis (crystal A, T2) are similar to the values for Z obtained from our previous bulk compaction experiments on wet granular halite, which yielded Z values in the range $6 \times 10^{-16} \text{ kg/s}$ to $6 \times 10^{-17} \text{ kg/s}$ for volumetric strains up to around 18% (Spiers *et al.*, 1990; Schutjens, 1991b; Spiers and Brzesowsky, 1993). Since most of our halite-halite convergence rate data fall near the “lower bound” rates obtained for crystal A of experiment T2 (Fig. 12), this increases our confidence in the interpretation that the IPS process observed in the present experiments involved diffusion-controlled transport of mass out of the crystal contacts parallel to their width, with the contact structure and effective diffusivity varying from experiment to experiment as well as with contact force and on-going convergence (contact smoothing with time). We suggest that the high (upper bound) Z values obtained from experiment T1 (contact A, Fig. 13) reflect the very rough/irregular contact structure developed in this sample (Fig. 8).

A tentative evaluation can now be made of the relationship between the intrinsic diffusivity of the solute in the grain boundary fluid (D , in m^2/s) and the effective grain boundary thickness (S , in m) using Equation (16): $Z = D \cdot C_0 \cdot S$. For the lower-bound value of Z of 10^{-16} kg/s , D takes a value of about $10^{-12} \text{ m}^2/\text{s}$ if we assume an effective

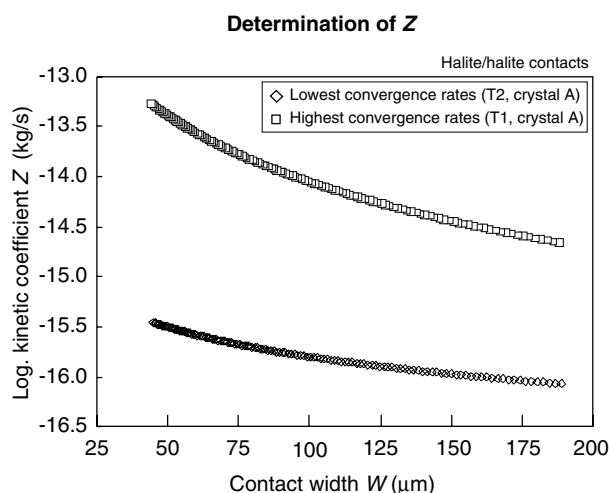


Figure 13

Plot of kinetic coefficient (Z) as a function of contact width (W) assuming grain boundary diffusion controlled intergranular pressure solution, with diffusion along the short edge of the contact face (Model A). The curves were calculated from Equation (11) using the upper and lower bound relations between \dot{X}/F and W obtained from Figure 12 (halite-halite contacts). Values of Z range from $4 \times 10^{-14} \text{ kg/s}$ to 10^{-16} kg/s for W in the range 50 to 175 μm , and reflect the wide range in crystal convergence rate observed at the halite-halite contacts. Note that the calculated values of Z decrease with increasing contact.

grain boundary thickness of 200 nm and normally saturated brine ($C_0 = 311 \text{ kg/m}^3$). This is about three orders of magnitude lower than the diffusivity of ionized NaCl in bulk solution (about $10^{-9} \text{ m}^2/\text{s}$; Kestin *et al.*, 1981). Taking higher values of Z will reduce this difference, but we think that our experimental data suggest that the intrinsic “grain boundary” diffusivity may be substantially lower than the diffusivity of ionized NaCl in bulk fluid, in agreement with earlier interpretations (Spiers and Schutjens, 1990; Spiers *et al.*, 1990; Schutjens, 1991b).

Despite the above reasoning, we cannot eliminate the possibility that the IPS process observed in the present experiments was *not* driven by normal stress differences ($\Delta\mu_{ps} \approx \Delta\sigma_n/\rho$), in the manner embodied by our models, but was driven by source-sink gradients in defect-stored energy related to *dissipative* plastic flow occurring at grain contacts. Contact stresses were certainly large enough to cause some work hardening plastic flow (Davidge and Pratt, 1964; Wanten *et al.*, 1996). However, since our experiments indicate that marginal dissolution effects were not important, except possibly on initial loading, a defect-stored energy-driven mechanism seems unlikely for the subsequent stages of on-going IPS. Nonetheless, strain energy presumably did play a key role in controlling the roughening process accompanying incremental increases of contact load.

6.3 Comparison with Results of Hickman and Evans

In a series of systematic and well-controlled experiments, Hickman and Evans (1991, 1992, 1995) measured deformation at the contacts between polished lenses of halite and polished plates of either halite or fused silica, loaded under saturated NaCl brine, with the aim of investigating the mechanism and kinetics of IPS. The experiments were carried out at 50°C, employing plano-convex halite lenses with a convex radius of around 10 cm (Fig. 14). The normal stresses applied to the contacts fell in the range 1 to 14 MPa and were therefore of the same order as those used in the present study. In Hickman and Evans' experiments, initial loading led to the formation of a circular contact spot, typically 500 μm in diameter, as a result of instantaneous elastic and plastic deformation. When halite lenses were pressed against halite plates, there was *no* subsequent time-dependent convergence by contact dissolution. Instead, the contacts gradually widened by several hundred micrometres (neck growth) and fluid inclusions formed within the growing contacts. In contrast, when halite and silica were pressed together, time-dependent convergence by contact dissolution *did* occur, and no fluid inclusions were formed. Hickman and Evans inferred that this convergence was due to IPS, involving thin film diffusion. By comparison with the model of Rutter (1976) for thin film IPS at a circular grain contact, they obtained $Z = 8 \times 10^{-17}$ kg/s to 4×10^{-16} kg/s, which agrees fairly well with our lower-bound values for Z . In the case of their halite-halite contacts, Hickman and Evans reasoned that neck growth and the development of permanent inclusions proved nonzero dihedral wetting angles, and they accordingly deduced that continuous fluid films cannot exist stably in the boundary between two halite crystals loaded under brine. Both the lack of convergence at halite-halite contacts under stress as well as the inferred absence of a connected brine phase within the halite-halite contacts contrast sharply with the experimental results obtained in the present study, and with the results and interpretations of our previous compaction experiments on wet granular halite (Spiers and Schutjens, 1990; Spiers *et al.*, 1990; Spiers and Brzesowsky, 1993).

In an attempt to explain the discrepancy between Hickman and Evans' results and those reported here, we now compare the two experimental set-ups (cf. Figs. 1 and 14), procedures and the available thermodynamic driving forces for solution transfer. Our experimental set-up differs from that of Hickman and Evans (1991, 1992, 1995) in a variety of respects. In particular, we used cleaved halite crystals, rather than polished lenses and plates, creating an edge-face contact geometry more closely resembling that developed in compacting halite aggregates (Spiers *et al.*, 1990). Another important procedural difference is that less care was taken in our experiments to remove surface damage from the crystals used, so that this may have been considerably greater than in the halite-halite experiments of Hickman and Evans.

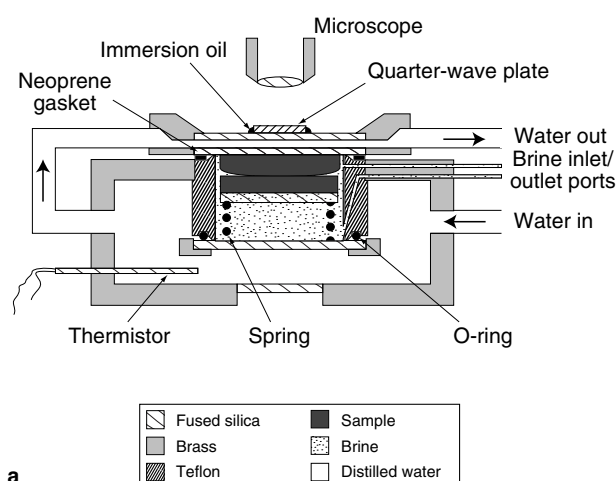


Figure 14a

Schematic diagram of the heated microscope stage/cell used in the contact dissolution experiments of Hickman and Evans (1991, 1992, 1995). Figure taken from Hickman and Evans (1995).

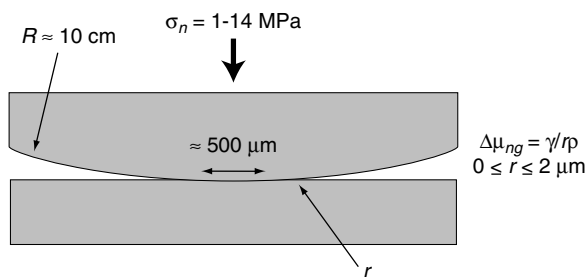


Figure 14b

Schematic enlargement of the lens-plate contact geometry used in the Hickman and Evans apparatus.

Focussing first on the geometric differences, a possible explanation for the neck growth at halite-halite contacts reported by Hickman and Evans lies in the large radius of curvature of their halite lenses. When pressed against a halite plate, the resulting configuration is characterized by an extremely sharp, negative radius of curvature (r) at the contact margin (Fig. 14b). Even for several hundred micrometres of neck growth, the contact geometry dictates that the magnitude of r will fall in the range $0 \mu\text{m}$ to $2 \mu\text{m}$ (see Hickman and Evans, 1991, 1992). Using the Gibbs-Thompson relation between chemical potential and surface curvature (Hickman and Evans, 1992), it follows that a chemical potential difference will exist between the free crystal surfaces and the contact margin, having magnitude $\gamma/r\rho$, where γ is the halite/brine interfacial energy ($\approx 0.3 \text{ J/m}^2$; estimated following Benson and Yun, 1965). This potential difference $\Delta\mu_{ng} \approx \gamma/r\rho$ represents the driving force for neck

growth, i.e. the driving force to transport mass from the free crystal surfaces to the contact margin, and for the range $0.01 \leq r \leq 2.0 \mu\text{m}$ takes values in the range $10^5/\rho$ to $3 \times 10^7/\rho$ J/kg. Note that these values are of similar order to the driving force for conventional pressure solution in the Hickman and Evans experiments, written $\Delta\mu_{ps} \approx \Delta\sigma_n/\rho$, since the normal stress applied to the contacts in their tests fell in the range 1 to 14 MPa. Increases in free energy and hence chemical potential at the contacts related to elastic or dislocation stored energy are negligible in comparison, being respectively of the order of $\sigma_n^2/2E\rho$ and $\sigma_n^2/G\rho$ (see Nabarro, 1987; Bosworth, 1981; Lehner and Bataille, 1984), i.e. of the order $10^1/\rho$ to $10^3/\rho$ J/kg.

Turning now to our halite-halite experiments (cf. Figs. 1b and 14b), the contact geometry is such that neck growth of only a few micrometres, as opposed to a few hundred micrometres, would increase the contact margin curvature r to values $> 2 \mu\text{m}$, quickly reducing the driving force $\Delta\mu_{ng}$ for neck growth to values $< 10^5/\rho$ J/kg. Thus in our halite-halite experiments, the driving force for sustained neck growth was far lower than in those of Hickman and Evans. We believe that this is the main reason why neck growth did not occur in our contact experiments (or indeed in our previous bulk compaction experiments on wet granular salt). On the basis of observations reported by Hickman and Evans (1991) for surface-damaged lenses, the neck growth process may have been further inhibited in the present experiments by surface damage effects related to our sample preparation method. The question remains, however, as to why the crystal contacts remained penetrated by brine throughout our halite-halite experiments and did not heal by internal neck or island growth occurring at solid-solid contact points (islands). At these points, the local (negative) radius of curvature is similar to the grain boundary thickness, so that the driving force for growth will be large. We suggest that such healing was prevented by microscale stress and strain energy concentrations and gradients developed within the contact, so that a dynamically wetted (nonequilibrium) contact structure was maintained. Presumably, at sufficiently low normal stresses, surface energy- or curvature-related driving forces would dominate over other terms, leading to healing of the contact structure in accordance with the nonzero dihedral angles obtained by Hickman and Evans (1992). An important challenge for future experimental and theoretical studies is thus to establish criteria defining the conditions under which such contact healing may occur (see also Lehner, 1990).

CONCLUSIONS

This study has shown that prismatic halite crystals loaded edgewise against the face of a cleaved (100) halite wafer or against a glass plate, in the presence of saturated brine, undergo time-dependent dissolution of material from the contact interface, at normal stresses in the range 1 to 7 MPa.

Initial application of normal stress to such contacts induces instantaneous formation of a rough contact morphology, composed of a crystallographically controlled pattern of islands and channels with a length scale of several micrometres, plus gradual convergence. The rough contact microstructure may form by internal dissolution within the contact, or possibly by a marginal dissolution or contact undercutting mechanism. It evolves with time and on-going convergence to form an optically flat contact face, with elongate inclusions. When contact stresses were increased, the optically smooth contact structure reroughened internally within minutes, presumably due to inhomogeneous plastic and/or elastic deformation, and the cycle of time-dependent convergence and gradual smoothing out of the contact structure repeated itself. The contacts were “wet”, in the sense that they contained an interconnected fluid phase. This was present within the rough contact structure or as a thin film, and allowed diffusive transport from the contact to the free fluid, causing the observed time-dependent convergence. No microstructural evidence was found for extensive plastic deformation or for brittle deformation at or near the contact interface. It is therefore concluded that the time-dependent convergence mainly occurred via an IPS mechanism.

Comparison of the present convergence data with models derived for grain boundary diffusional IPS suggests that the observed IPS process may have involved diffusion-controlled transport out of the crystal contacts parallel to their width, with the contact structure and effective diffusivity varying from experiment to experiment as well as with contact force and on-going convergence (contact smoothing with time). Fitting of the data for the halite-halite contacts to the appropriate model gives values for the kinetic coefficient Z of 10^{-16} kg/s to 4×10^{-14} kg/s, with most values clustering at the lower end. The lower values around 10^{-16} kg/s are of the same order of magnitude as the values for Z obtained from our previous bulk compaction experiments on wet halite powder ($Z = 6 \times 10^{-17}$ kg/s to 6×10^{-16} kg/s) and as the values obtained by Hickman and Evans (1991, 1992, 1995) in their halite-silica contact dissolution tests ($Z = 8 \times 10^{-17}$ kg/s to 4×10^{-16} kg/s). However, the results are quite different from the halite-halite contact experiments reported by Hickman and Evans, which showed neck growth at grain contacts instead of IPS. The discrepancy can be explained in terms of differences in experimental configuration, driving force for neck growth and competition between strain energy and surface energy driving forces.

ACKNOWLEDGMENTS

We thank Maurice Boutéca and Yves Guéguen for organizing the Euroconference 1998, and an anonymous reviewer for useful suggestions to improve this paper.

REFERENCES

- Angevine, C.L., Turcotte, D.L. and Furnish, M.D. (1982) Pressure Solution Lithification as a Mechanism for the Stick-Slip Behaviour of Faults. *Tectonics*, **1**, 151-160.
- Bathurst, R.C.G. (1958) Diagenetic Fabrics in some British Dinantian Limestones. *Liverpool and Manchester Geology*, **2**, 11-36.
- Bell, T.H. and Cuff, C. (1989) Dissolution, Solution Transfer, Diffusion Versus Fluid Flow and Volume Loss During Deformation/Metamorphism. *J. Metamorphic Geol.*, **7**, 425-447.
- Benson, G.C. and Yun, K.S. (1965) Surface Energies of Crystalline Solids. *J. Chem. Phys.*, **42**, 3085-3099.
- Boer de, R.B., Nagtegaal, P.J.C. and Duyvis, E.M. (1977) Pressure Solution Experiments on Quartz Sand. *Geochim. Cosmochim. Acta*, **41**, 257-264.
- Bosworth, W. (1981) Strain-Induced Preferential Dissolution of Halite. *Tectonophysics*, **78**, 349-369.
- Carozzi, A.V. and von Bergen, D. (1987) Stylolitic Porosity in Carbonates: A Critical Factor for Deep Hydrocarbon Production. *J. Petrol. Geol.*, **10**, 267-282.
- Cox, S.F. and Paterson, M. (1991) Experimental Dissolution-Precipitation Creep in Quartz Aggregates at High Temperatures. *Geophys. Res. Lett.*, **18**, 1401-1404.
- Davidge, R.W. and Pratt, P.L. (1964) Plastic Deformation and Work-Hardening in NaCl. *Phys. Stat. Sol.*, **6**, 759-776.
- Denbigh, R. (1971) *The Principles of Chemical Equilibrium*, Cambridge Univ. Press (3rd edition).
- Dewers, T. and Hajash, A. (1995) Rate Laws for Water-Assisted Densification and Stress-Induced Water-Rock Interaction in Sandstones. *USGS Open File Report 94-228. The Mechanical Involvement of Fluids in Faulting*, USGS Menlo Park, Ca. 1994, Hickman, S., Sibson, R. and Brahm R. (eds.).
- Gratz, A.J. (1991) Solution-Transfer Compaction of Quartzites: Progress Toward a Rate Law. *Geology*, **19**, 901-904.
- Hickman, S.H. and Evans, B. (1991) Experimental Pressure Solution in Halite: The Effect of Grain/Interphase Boundary Structure. *J. Geol. Soc. Lond.*, **148**, 549-560.
- Hickman, S.H. and Evans, B. (1992) Growth of Grain Contacts in Halite by Solution-Transfer: Implications for Diagenesis, Lithification and Strength Recovery. In: *Fault Mechanics and Transport Properties of Rocks*, Evans, B. and Wong, T.F. (eds.), Academic Press, San Diego USA, 253-280.
- Hickman, S.H. and Evans, B. (1995) Kinetics of Pressure Solution at Halite-Silica Interfaces and Intergranular Films. *J. Geophys. Res.*, **B7**, 100, 13113-13132.
- Houseknecht, D.W. (1984) Influence of Grain Size and Temperature on Intergranular Pressure Solution, Quartz Cementation, and Porosity in a Quartzose Sandstone. *J. Sediment. Petrol.*, **54**, 348-361.
- Houseknecht, D.W. (1987) Assessing the Relative Importance of Compaction Processes and Cementation to Reduction of Porosity in Sandstones. *Bull. Am. Ass. Petrol. Geol.*, **71**, 633-642.
- Houseknecht, D.W. (1988) Intergranular Pressure Solution in Four Quartzose Sandstones. *J. Sediment. Petrol.*, **58**, 228-246.
- Hutcheon, I. (1983) Aspects of Diagenesis of Coarse Grained Siliciclastic Rocks. *Geoscience Canada*, **10**, 4-14.
- Kamb, W.B. (1959) Theory of Preferred Crystal Orientation Developed by Crystallisation under Stress. *J. Geology*, **67**, 153-170.
- Kestin, J., Khalifa, H.E. and Correia, J. (1981) Tables of the Dynamic and Kinematic Viscosity of Aqueous NaCl-Solution in the Temperature Range 20-150°C and Pressure Range 0.1-35 MPa. *J. Phys. Chem. Ref. Data*, **10**, 71-87.
- Lehner, F.K. and Bataille, J. (1984/85) Non-Equilibrium Thermodynamics of Pressure-Solution. *Pure Appl. Geophys.*, **122**, 53-85.
- Lehner, F.K. (1990) Thermodynamics of Rock Deformation by Pressure Solution. In: *Deformation Processes in Minerals, Ceramics and Rocks.*, Barber, D.J. and Meredith, P.D. (eds.) Unwin Hyman, 296-333.
- Lehner, F.K. (1995) A Model for Intergranular Pressure Solution in Open Systems. In: *Influence of Fluids on Deformation Processes in Rocks.*, Spiers, C.J. and Takeshita, T. (eds.). *Tectonophysics*, **245**, 153-170.
- Mullis, A. (1991) The Role of Silica Precipitation Kinetics in Determining the Rate of Quartz Pressure Solution. *J. Geophys. Res.*, **96**, 10007-10013.
- Nabarro, F.R.N. (1987) *Theory of Crystal Dislocations*, Dover, New York.
- Paterson, M.S. (1995) A Theory for Granular Flow Accommodated by Material Transfer via an Intergranular Fluid. In: *Influence of Fluids on Deformation Processes in Rocks.*, Spiers, C.J. and Takeshita, T. (eds.). *Tectonophysics*, **245**, 135-151.
- Pharr, G.M. and Ashby, M.F. (1983) On Creep Enhanced by a Liquid Phase. *Acta Metall.*, **31**, 129-138.
- Pittman, E.D. (1979) Porosity, Diagenesis and Productive Capability of Sandstone Reservoirs. *Soc. Econ. Pal. Min. Spec. Publ.*, **26**, 159-173.
- Raj, R. (1982) Creep in Polycrystalline Aggregates by Matter Transport Through a Liquid Phase. *J. Geophys. Res.*, **87**, 4731-4739.
- Renton, J.J., Heald, M.T. and Cecil, C.B. (1969) Experimental Investigation of Pressure Solution of Quartz. *J. Sediment. Petrol.*, **39**, 1107-1117.
- Rutter, E.H. (1976) The Kinetics of Rock Deformation by Pressure Solution. *Phil. Trans. R. Soc. Lond.*, **A283**, 203-219.
- Rutter, E.H. (1983) Pressure Solution in Nature, Theory and Experiment. *J. Geol. Soc. Lond.*, **140**, 725-740.
- Rutter, E.H. and Mainprice, D.H. (1978) On the Possibility of Slow Fault Slip Controlled by a Diffusive Mass Transfer Process. *Gerlands Beitr. Geophysik, Leipzig*, **88**, 2, 154-162.
- Schutjens, P.M.T.M. (1991a) Experimental Compaction of Quartz Sand at Low Effective Stress and Temperature Conditions. *J. Geol. Soc. Lond.*, **148**, 527-539.
- Schutjens, P.M.T.M. (1991b) Intergranular Pressure Solution in Halite Aggregates and Quartz Sands: An Experimental Investigation. Doctoral Dissertation, Faculty of Earth Sciences, Utrecht University. *Geol. Ultraiectina*, **76**.
- Shimizu, I. (1995) Kinetics of Pressure Solution Creep in Quartz: Theoretical Considerations. *Tectonophysics*, **245**, 121-134.
- Sleep, N.H. (1995) Ductile Creep, Compaction, and Rate and State Dependent Friction within Major Fault Zones. *J. Geophys. Res.*, **100**, 13065-13080.
- Sleep, N.H. and Blanpied, M.L. (1992) Creep, Compaction and the Weak Rheology of Major Faults. *Nature*, **359**, 687-692.
- Spiers, C.J., Lister, G.S., Boland, J.N. and Zwart, H.J. (1986) The Influence of Fluid-Rock Interaction on the Rheology of Salt Rock. Final Report. *Nuclear Science and Technology*, EUR 10399 EN.
- Spiers, C.J., Peach, C.J., Brzesowsky, R.H., Schutjens, P.M.T.M., Liezenberg, J.L. and Zwart, H.J. (1989) Long-Term Rheological and Transport Properties of Dry and Wet Salt Rocks. *Nuclear Science and Technology*, EUR 11848 EN, Office for Official Publications of the European Communities, Luxembourg.
- Spiers, C.J., Schutjens, P.M.T.M., Brzesowsky, R.H., Peach, C.J., Liezenberg, J.L. and Zwart, H.J. (1990) Experimental

- Determination of Constitutive Parameters Governing Creep of Rocksalt by Pressure Solution. In: *Deformation Mechanisms, Rheology and Tectonics*, Knipe, R. and Rutter, E.H. (eds.). *J. Geol. Soc. Spec. Publ.*, 54, 215-227.
- Spiers, C.J. and Schutjens, P.M.T.M. (1990) Densification of Crystalline Aggregates by Fluid-Phase Diffusional Creep. In: *Deformation Processes in Minerals, Ceramics and Rocks*. Barber, D.J. and Meredith, P.D. (eds.). Unwin Hyman, 334-353.
- Spiers, C.J. and Brzesowsky, R.H. (1993) Densification Behaviour of Wet Granular Salt: Theory Versus Experiment. In: *Seventh Symposium on Salt*. Elsevier, Amsterdam, 1, 83-92.
- Tada, R., Maliva, R. and Siever, R. (1987) A New Mechanism for Pressure Solution in Porous Quartzose Sandstone. *Geochim. Cosmochim. Acta.*, 51, 2295-2301.
- Tada, R. and Siever, R. (1989) Pressure Solution During Diagenesis. *Ann. Rev. Earth Planet Sci.*, 17, 89-118.
- Taylor, J.M. (1950) Pore-Space Reduction in Sandstones. *Bull. Am. Assoc. Petrol. Geol.*, 34, 701-716.
- Urai, J.L., Spiers, C.J., Zwart, H.J. and Lister, G.S. (1986) Weakening of Rocksalt by Water During Long-Term Creep. *Nature*, 324, 554-557.
- Wanten, P.H., Spiers, C.J. and Peach, C.J. (1996) Deformation of NaCl Single Crystals at $0.27 T_m \leq T \leq 0.44 T_m$. In: *The Mechanical Behavior of Salt, Proc. 3rd Conf., Trans Tech Publ., Series on Rock and Soil Mechanics*, Ghoreychi, M., Berest, P., Hardy Jr, H.R. and Langer, M. (eds.), 20, 117-128.
- Weyl, P.K. (1959) Pressure Solution and Force of Crystallization—a Phenomenological Theory. *J. Geophys. Res.*, 64, 2001-2025.

Final manuscript received in July 1999